

1                   **Rheologic constraints on the upper mantle from five years of**  
2                   **postseismic deformation following the El Mayor-Cucapah**  
3                   **earthquake**

4                   **T. T. Hines<sup>1</sup>, E. A. Hetland<sup>1</sup>**

5                   <sup>1</sup>Department of Earth and Environmental Sciences, University of Michigan, Ann Arbor, Michigan, USA.

6                   **Key Points:**

- 7                   • Transient postseismic deformation can be observed following the El Mayor-Cucapah  
8                   earthquake at epicentral distances of up to 400 km  
9                   • Near-field postseismic deformation exhibits early transience that decays to a sustained  
10                  rate which is elevated above the preseismic trend  
11                  • A Zener or Burgers upper mantle can explain far-field deformation while near-field tran-  
12                  sience can be described with afterslip

13 **Abstract**

14 Five years of postseismic deformation following the Mw7.2 El Mayor-Cucapah earthquake re-  
 15 veals transient deformation that decays back to its pre-earthquake trend after about three years  
 16 at epicentral distances greater than  $\sim 200$  km. At closer distances, the rapid transience decays  
 17 to a sustained rate which exceeds its pre-earthquake trend. We attempt to determine the mech-  
 18 anisms driving this deformation, where we consider afterslip at seismogenic depths and vis-  
 19 coelastic relaxation in the lower crust and upper mantle as candidate mechanisms. We find that  
 20 early, rapid, near-field deformation can be explained with afterslip on the fault that ruptured  
 21 coseismically, while the later, sustained, near-field deformation can be explained with either  
 22 continued afterslip in an effectively elastic lower crust, or lower crustal viscoelastic relaxation  
 23 with a steady-state viscosity of  $\sim 10^{19}$  Pa s. The trend in far-field deformation is best explained  
 24 with a transient viscosity of  $\sim 10^{18}$  Pa s in the upper mantle. We argue that a transient rhe-  
 25 ology in the mantle is preferable over a Maxwell rheology because it better predicts the de-  
 26 cay in postseismic deformation, and also because it does not conflict with the generally higher,  
 27 steady-state viscosities inferred from studies of geophysical processes occurring over longer  
 28 time-scales.

29 **1 Introduction**

30 Ground deformation in the years following a large ( $\gtrsim$ Mw7) earthquake provides insight  
 31 into the mechanical behavior of the crust and upper mantle. It has long been recognized that  
 32 interpretations of postseismic deformation can be ambiguous because multiple postseismic de-  
 33 formation mechanisms can have qualitatively similar surface expressions [e.g. Savage, 1990].  
 34 Owing to the dense geodetic network deployed throughout the 2000s as part of the Plate Bound-  
 35 ary Observatory, the postseismic deformation following the April 4, 2010, Mw7.2 El Mayor-  
 36 Cucapah earthquake in Baja California was observed at more GPS stations than any other earth-  
 37 quake in California to date. With such a large collection of data, we attempt to discern the mech-  
 38 anisms driving postseismic deformation following the El Mayor-Cucapah earthquake, where  
 39 we consider both afterslip and viscoelastic relaxation in the lower crust and upper mantle as  
 40 candidate mechanisms.

41 Previous studies which have modeled postseismic deformation following the El Mayor-  
 42 Cucapah earthquake include Pollitz *et al.* [2012], Gonzalez-Ortega *et al.* [2014], Spinler *et al.*  
 43 [2015], and Rollins *et al.* [2015]. Of these studies, Gonzalez-Ortega *et al.* [2014] and Rollins  
 44 *et al.* [2015] have attempted to describe the postseismic deformation with afterslip in an elas-  
 45 tic half-space. Gonzalez-Ortega *et al.* [2014] described five months of postseismic deforma-  
 46 tion, observed by InSAR and GPS within  $\sim 50$  km of the rupture, with afterslip and contrac-  
 47 tion on the coseismically ruptured fault. Gonzalez-Ortega *et al.* [2014] noted that their preferred  
 48 model underestimated the GPS displacements for stations  $\gtrsim 25$  km from the rupture and sug-  
 49 gested that it could be the result of unmodeled viscoelastic relaxation. Using only continuous  
 50 GPS stations, which are mostly north of the rupture zone, Rollins *et al.* [2015] found that three  
 51 years of postseismic deformation can be adequately explained by afterslip, albeit with an im-  
 52 plausibly large amount of slip inferred on the least constrained, southern-most fault segment.  
 53 Here, we suggest the afterslip inferred by Rollins *et al.* [2015] may have been acting as a proxy  
 54 for distributed relaxation in the upper mantle.

55 Pollitz *et al.* [2012], Rollins *et al.* [2015] and Spinler *et al.* [2015] have explored viscoelas-  
 56 tic relaxation in the lower crust and upper mantle as a potential postseismic deformation mech-  
 57 anism. The rheology of the crust and mantle is largely unknown and so modeling postseis-  
 58 mic deformation with viscoelastic relaxation requires one to assume a rheologic model and  
 59 then find the best fitting rheologic parameters. The inference of these rheologic parameters is  
 60 a computationally expensive non-linear inverse problem which is typically approached with  
 61 a forward modeling grid search method. Consequently, a simplified structure for the Earth must  
 62 be assumed in order to minimize the number of rheologic parameters that need to be estimated.  
 63 For example, it is commonly assumed that the lower crust and upper mantle are homogeneous,

Maxwell viscoelastic layers, which may be too simplistic for postseismic studies [Riva and Govers, 2009; Hines and Hetland, 2013]. To further reduce the dimensions of the model space, it is also necessary to make simplifying assumptions about the nature of afterslip. For example, one can assume a frictional model for afterslip and parametrize afterslip in terms of the unknown rheologic properties of the fault [e.g. Johnson *et al.*, 2009; Johnson and Segall, 2004]. One can also assume that afterslip does not persist for more than a few months and then model the later postseismic deformation assuming it to be the result of only viscoelastic relaxation [e.g. Pollitz *et al.*, 2012; Spinler *et al.*, 2015]. However, postseismic afterslip in similar tectonic settings has been observed to persist for decades following earthquakes [Çakir *et al.*, 2012; Cetin *et al.*, 2014]. Indeed, the preferred viscoelastic model from Pollitz *et al.* [2012] significantly underestimates deformation in the Imperial Valley, which could be indicative of unmodeled continued afterslip. Neglecting to allow for sustained afterslip as a postseismic mechanism could then lead to biased inferences of viscosities.

In this study, we perform a kinematic inversion for fault slip, allowing it to persist throughout the postseismic period, while simultaneously estimating the viscosity of the lower crust and upper mantle. We create an initial model of the fault slip and effective viscosity necessary to describe early postseismic deformation using the method described in Hines and Hetland [2016]. This method utilizes a first-order approximation of surface deformation resulting from viscoelastic relaxation which is only applicable to the early postseismic period. In this case, our initial model describes the first 0.8 years of postseismic deformation following the El Mayor-Cucapah earthquake. We then use the inferred effective viscosity structure from the initial model to create a suite of postseismic models to explain the five years of postseismic data available to date. Of the suite of models tested, we find that postseismic deformation following the El Mayor-Cucapah earthquake can be explained with a combination of afterslip on a fault segment running through the Sierra Cucapah and a Zener rheology in the upper mantle with a transient viscosity that decays from  $6 \times 10^{18}$  Pa s to  $1 \times 10^{18}$  Pa s at 120 km depth.

## 2 Data Processing

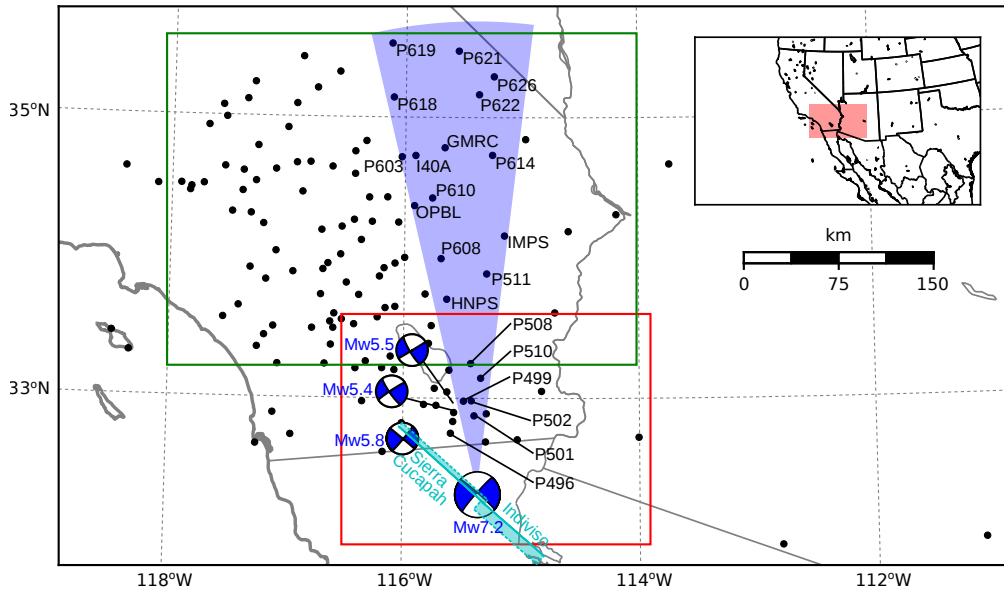
We use continuous GPS position time series provided by University Navstar Consortium (UNAVCO) for stations within a 400 km radius about the El Mayor-Cucapah epicenter. We collectively describe the coseismic and postseismic displacements resulting from the El Mayor-Cucapah earthquake as  $u_{\text{post}}(t)$ . We consider the GPS position time series  $u_{\text{obs}}(t)$  to be the combination of  $u_{\text{post}}(t)$ , secular tectonic deformation, annual and semi-annual oscillations, and coseismic offsets from significant earthquakes over the time span of this study. The June 14, 2010, Mw5.8 Ocotillo earthquake and the Brawley swarm, which included an Mw5.5 and an Mw5.4 event on August 26, 2012, (Figure 1) are the only earthquakes that produced noticeable displacements in any of the time series. We treat the displacements resulting from the Brawley swarm as a single event because the daily solutions provided by UNAVCO cannot resolve the separate events. Although the Ocotillo earthquake had its own series of aftershocks [Hauksson *et al.*, 2011], neither the Ocotillo earthquake nor the Brawley swarm produced detectable postseismic deformation. We model displacements resulting from these events with only a Heaviside function,  $H(t)$ , describing the coseismic offsets. We then model  $u_{\text{obs}}(t)$  as

$$u_{\text{obs}}(t) = u_{\text{pred}}(t) + \epsilon, \quad (1)$$

where

$$\begin{aligned} u_{\text{pred}}(t) = & u_{\text{post}}(t)H(t - t_{\text{emc}}) + c_0 + c_1 t + \\ & c_2 \sin(2\pi t) + c_3 \cos(2\pi t) + c_4 \sin(4\pi t) + c_5 \cos(4\pi t) + \\ & c_6 H(t - t_{\text{oc}}) + c_7 H(t - t_{\text{bs}}). \end{aligned} \quad (2)$$

In the above equations,  $t_{\text{emc}}$ ,  $t_{\text{oc}}$  and  $t_{\text{bs}}$  are the times of the El Mayor-Cucapah earthquake, Ocotillo earthquake, and the Brawley swarm, respectively,  $c_0$  through  $c_7$  are unknown coefficients, and  $\epsilon$  is the observation noise. We only estimate jumps associated with the Ocotillo earthquake and Brawley swarm for stations within 40 km of their epicenters.



91 **Figure 1.** Map of the region considered in this study. The large focal mechanism is for the El Mayor-  
92 Cucapah earthquake, and the three small focal mechanisms are for the Ocotillo earthquake and the two main  
93 shocks during the Brawley swarm. The black dots indicate the locations of GPS stations used in this study.  
94 The fault geometry used in this study is shown in cyan where dashed lines indicate buried edges of the fault  
95 segments. The green and red boxes demarcate the extent of the near-field and far-field maps (Figures 4 and 5).  
96 Stations inside the blue sector, which highlights the area within  $10^{\circ}$  of the El Mayor-Cucapah P axis, are used  
97 in Figures 7, 10, and 14

103 Stations which recorded displacements that clearly cannot be described by the aforementioned  
 104 processes are not included in our analysis. This includes stations in the Los Angeles  
 105 basin, where anthropogenic deformation can be larger than the postseismic signal that we are  
 106 trying to estimate [Bawden *et al.*, 2001; Argus *et al.*, 2005]. In order to ensure an accurate es-  
 107 timation of the secular deformation, we only use stations that were installed at least six months  
 108 prior to El Mayor-Cucapah earthquake. Several GPS stations were installed after the El Mayor-  
 109 Cucapah earthquake to improve the spatial resolution of postseismic deformation [Spinler *et al.*,  
 110 2015]. Although it would be possible to subtract secular velocities derived from elastic block  
 111 models [e.g. Meade and Hager, 2005] from velocities recorded at the newly installed stations  
 112 to get an estimate of postseismic velocities, we do not do so here. We use coseismic and post-  
 113 seismic displacements, rather than velocities, in our inverse method described in Section 3. We  
 114 use displacements because estimating velocities from an already noisy displacement time se-  
 115 ries can introduce significant uncertainties depending on exactly how the estimation is done.  
 116 This choice prevents us from using the newly installed stations in Baja California for our anal-  
 117 ysis.

118 The October 16, 1999, Mw7.1 Hector Mine earthquake, which occurred  $\sim$ 270 km north  
 119 of the El Mayor-Cucapah epicenter, produced transient postseismic deformation which we do  
 120 not wish to model, either mechanically or through empirical line fitting. We thus restrict our  
 121 analysis to deformation observed six years after the Hector Mine earthquake, which is when  
 122 postseismic velocities at sites proximal to the Hector Mine epicenter are approximately con-  
 123 stant [Savage and Svare, 2009]. When appraising our model fit in Section 3, we see some sys-  
 124 tematic residuals in the vicinity of the Hector Mine epicenter, which may be the result of er-  
 125 rors in the assumption that the trend in Hector Mine postseismic deformation is linear after  
 126 six years.

Studies of postseismic deformation typically assume a parametric form for  $u_{\text{post}}(t)$ , such as one with a logarithmic or exponential time dependence [e.g. Savage *et al.*, 2005]. However, by assuming a logarithmic or exponential form of  $u_{\text{post}}(t)$  we run the risk of over fitting the GPS time series and inferring a non-existent postseismic signal. We therefore do not assume any parametric form for  $u_{\text{post}}(t)$  and rather treat it as integrated Brownian motion, so that

$$\dot{u}_{\text{post}}(t) = \sigma^2 \int_0^t w(s) ds, \quad (3)$$

where  $w(t)$  is white noise and the variance of  $\dot{u}_{\text{post}}(t)$  increases linearly with time by a factor of  $\sigma^2$ . We use a Kalman filtering approach to estimate  $u_{\text{post}}(t)$  and the unknown parameters in eq. (2). In the context of Kalman filtering, our time varying state vector is

$$\mathbf{X}(t) = [u_{\text{post}}(t), \dot{u}_{\text{post}}(t), c_0, \dots, c_7] \quad (4)$$

and eq. (2) is the observation function which maps the state vector to the GPS observations. We initiate the Kalman filter by assuming a prior estimate of  $\mathbf{X}(t)$  at the first time epoch, denoted  $\mathbf{X}_{1|0}$ , which has a sufficiently large covariance, denoted  $\Sigma_{1|0}$ , to effectively make our prior uninformed. For each time epoch  $t_i$ , Bayesian linear regression is used to incorporate GPS derived estimates of displacement with our prior estimate of the state  $\mathbf{X}_{i|i-1}$  to form a posterior estimate of the state  $\mathbf{X}_{i|i}$ , which has covariance  $\Sigma_{i|i}$ . We then use the posterior estimate of the state at time  $t_i$  to form a prior estimate of the state at time  $t_{i+1}$  through the transition function

$$\mathbf{X}_{i+1|i} = \mathbf{F}_{i+1} \mathbf{X}_{i|i} + \delta_{i+1}, \quad (5)$$

where

$$\mathbf{F}_{i+1} = \begin{bmatrix} 1 & (t_{i+1} - t_i) & \mathbf{0} \\ 0 & 1 & \mathbf{0} \\ \mathbf{0} & \mathbf{0} & \mathbf{I} \end{bmatrix} \quad (6)$$

and  $\delta_{i+1}$  is the process noise, which has zero mean and covariance described by

$$\mathbf{Q}_{i+1} = \sigma^2 \begin{bmatrix} \frac{(t_{i+1}-t_i)^3}{3} & \frac{(t_{i+1}-t_i)^2}{2} & \mathbf{0} \\ \frac{(t_{i+1}-t_i)^2}{2} & (t_{i+1} - t_i) & \mathbf{0} \\ \mathbf{0} & \mathbf{0} & \mathbf{0} \end{bmatrix}. \quad (7)$$

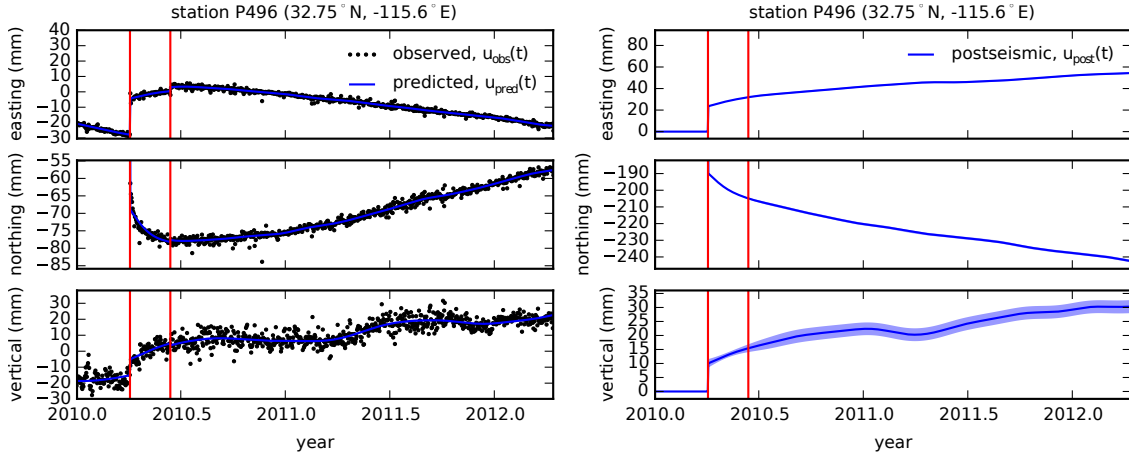


**Figure 2.** Left panels show GPS time series from UNAVCO (black) and the predicted displacement (blue) from eq. (2) for a near-field station. Red lines indicate the times of the El Mayor-Cucapah and Ocotillo earthquake. The right panels show estimated coseismic and postseismic displacements  $u_{\text{post}}$  which are extracted from the predicted displacements. The 68% confidence interval is shown in light blue.

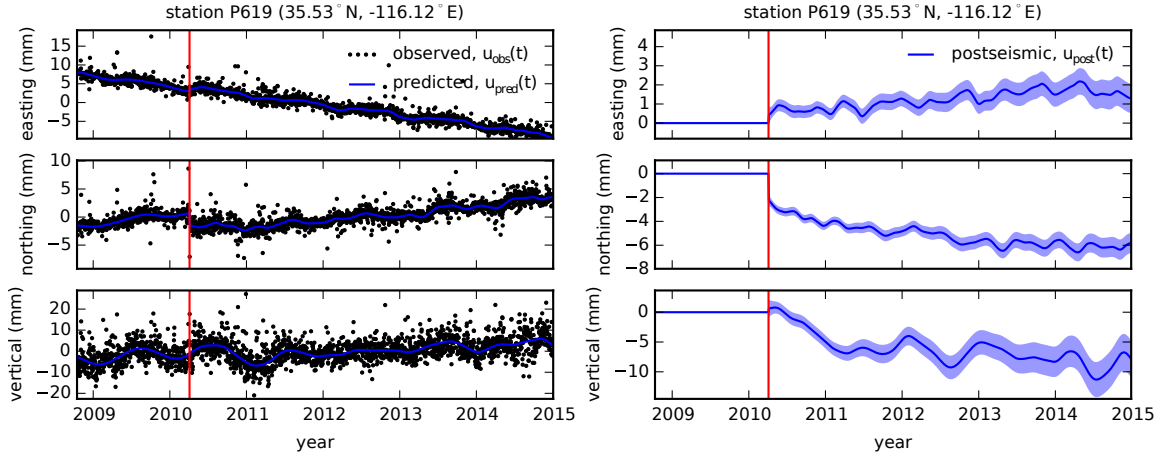
The covariance of the new prior state,  $\mathbf{X}_{i+1|i}$ , is then described by

$$\Sigma_{i+1|i} = \mathbf{F}_{i+1} \Sigma_{i|i} \mathbf{F}_{i+1}^T + \mathbf{Q}_{i+1}. \quad (8)$$

This process is repeated for each of the  $N$  time epochs at which point we use Rauch-Tung-Striebel smoothing [Rauch *et al.*, 1965] to find  $\mathbf{X}_{i|N}$ , which is an estimate of the state at time  $t_i$  that incorporates GPS observation for all  $N$  time epochs. Our final estimates of  $u_{\text{post}}(t)$  are used in subsequent analysis, while the remaining components of the state vector are considered nuisance parameters. In the interests of computational tractability, we down sample our smoothed time series from daily solutions down to weekly solutions.

The smoothness of  $u_{\text{post}}(t)$  is controlled by the chosen value of  $\sigma^2$ , which describes how rapidly we expect postseismic displacements to vary over time. Setting  $\sigma^2$  equal to zero will effectively result in modeling  $u_{\text{post}}(t)$  as a straight line which is insufficient to describe the expected transient behavior in postseismic deformation. The other end member, where  $\sigma^2$  is infinitely large, will result in  $u_{\text{pred}}(t)$  over fitting the data. While one can use a maximum likelihood based approach for picking  $\sigma^2$  [e.g. Segall and Mathews, 1997], we instead take a subjective approach and choose a value for  $\sigma^2$  that is just large enough to faithfully describe the observed deformation at the most near-field station in our study, P496, which exhibits the most pronounced rapid changes in velocity. This ensures that  $\sigma^2$  will be sufficiently large so that our estimate of  $u_{\text{post}}(t)$  does not smooth out potentially valuable postseismic signal at the remaining stations. We find that using  $\sigma^2 = 0.05 \text{ m}^2/\text{yr}^3$  adequately describe all but the first week of postseismic deformation at station P496, which gets incorporated into our estimate of coseismic displacements (Figure 2). We assume that the first week of deformation is overwhelmingly the result of afterslip and this afterslip is lumped into our estimates of coseismic slip. Freed *et al.* [2007] noted that postseismic deformation can be observed at distances greater than 200 km from the Hector Mine earthquake and, after filtering the time series for stations up to 400 km from the El Mayor-Cucapah epicenter, we also clearly see far reaching postseismic transient deformation (Figure 3).

It is important to note that the shown uncertainties in  $u_{\text{post}}(t)$  do not account for the non-negligible epistemic uncertainty in eq. (2). For example, we assume a constant rate of secular deformation, which appears to be an appropriate approximation for all but perhaps the stations closest to the Hector Mine epicenter, as noted above. Also, our model for seasonal de-

155 **Figure 3.** same as Figure 2 but for a far-field station.

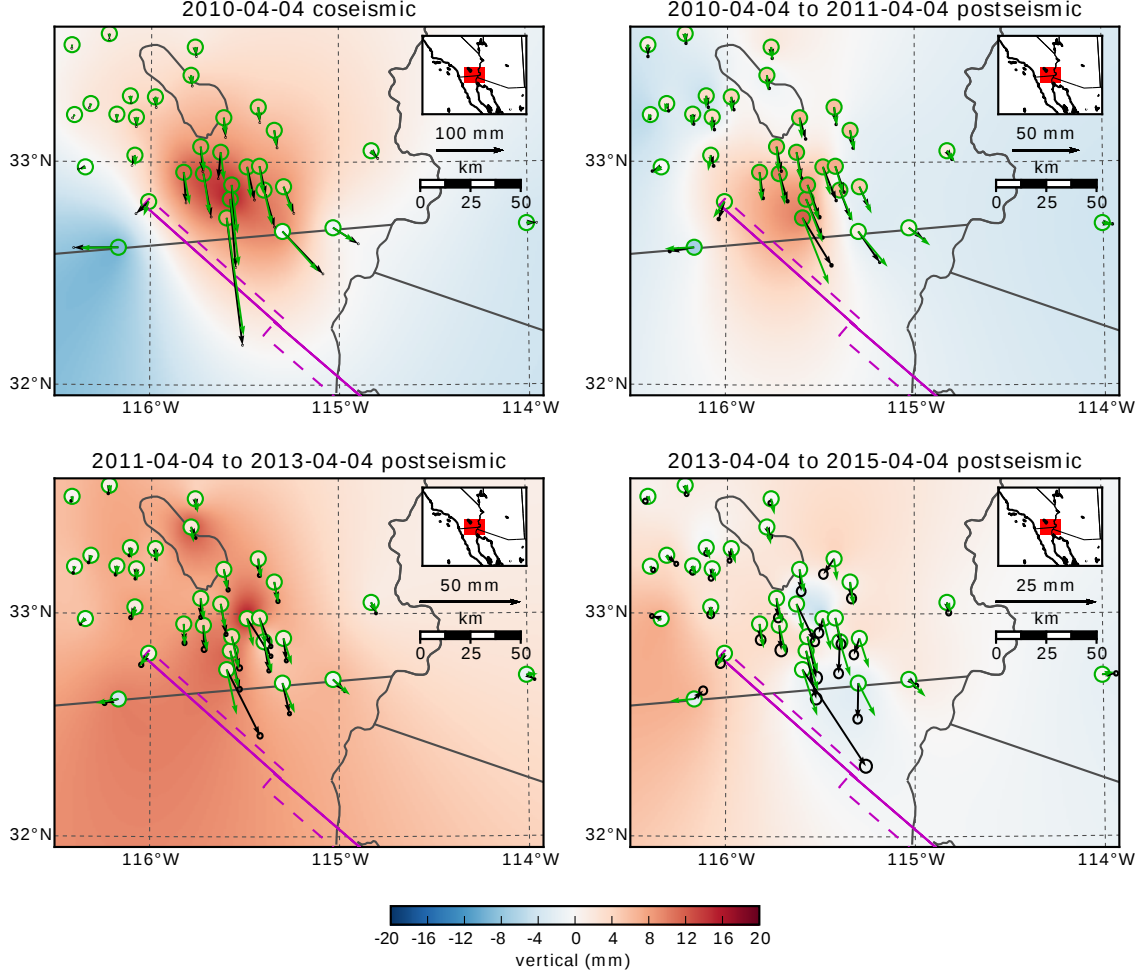
160 formation in eq. (2) assumes a constant amplitude over time, which means that any yearly vari-  
 161 ability in the climatic conditions could introduce systematic residuals [Davis *et al.*, 2012]. In-  
 162 deed, it would be more appropriate to consider the seasonal amplitudes  $c_2 - c_5$  in eq. (2) as  
 163 stochastic variables [Murray and Segall, 2005]. By using constant seasonal amplitudes, our es-  
 164 timate of  $u_{\text{post}}(t)$  seems to describe some of the unmodeled annual and semi-annual oscilla-  
 165 tions (e.g. Figure 3).

166 We show in Figures 4 and 5 the near and far-field postseismic displacements accumu-  
 167 lated over the time intervals 0-1 years, 1-3 years, and 3-5 years, as well as the coseismic dis-  
 168 placements. Stations at epicentral distances beyond  $\sim 200$  km have an elevated rate of defor-  
 169 mation for the first three years following the earthquake. This far-field deformation has a south-  
 170 ward trend along the direction of the El Mayor-Cucapah P axis and a similar eastward trend  
 171 can be seen in the few far-field stations in Arizona, located along the T axis. After three years,  
 172 the trend in far-field postseismic deformation is barely perceptible. Most far-field stations dis-  
 173 play an initial subsidence for the first year after the El Mayor-Cucapah earthquake followed  
 174 by continued uplift. This trend in vertical deformation can be observed in all three of the quad-  
 175 rants where postseismic data is available, which means that the vertical deformation does not  
 176 exhibit an anti-symmetric quadrant pattern, as would be expected for postseismic processes.  
 177 Although we use vertical deformation in our analysis in Section 3, we do not put an empha-  
 178 sis on trying to describe the vertical deformation as it likely does not have postseismic ori-  
 179 gins.

186 The near-field postseismic deformation is notably sustained when compared to the far-  
 187 field deformation. Namely, the station in this study which is closest to the El Mayor-Cucapah  
 188 epicenter, P496, has been moving at a steady rate of  $\sim 1.5$  cm/yr to the south since about one  
 189 year after the El Mayor-Cucapah earthquake. Vertical postseismic deformation in the near-field  
 190 does display a quadrant pattern which is consistent with the coseismic vertical deformation,  
 191 suggesting that it is resulting from postseismic processes. However, the vertical postseismic  
 192 signal is only apparent for the first year after the earthquake (Figure 4). As with the far-field  
 193 deformation, there is a general trend of uplift in the near-field after about one year.

### 194 3 Postseismic Modeling

198 We seek to find the mechanisms driving five years of postseismic deformation follow-  
 199 ing the El Mayor-Cucapah earthquake and we consider afterslip and viscoelastic relaxation as  
 200 candidate mechanisms. Poroelastic rebound has also been used to model postseismic defor-  
 201 mation [e.g. Jónsson *et al.*, 2003]; however, Gonzalez-Ortega *et al.* [2014] found that poroe-



180 **Figure 4.** Near-field coseismic and cumulative postseismic displacements over the indicated time periods  
 181 (black) as well as predicted displacements for our preferred model from Section 3.3 (green). Observed vertical  
 182 deformation is shown as an interpolated field and predicted vertical displacements are shown within the  
 183 circles at the base of each vector. Note that the interpolant is not well constrained in Mexico where there is no  
 184 data available.

depth (km)	$\lambda$ (GPa)	$\mu$ (GPa)	$\eta_{\text{eff}}$ ( $10^{18}$ Pa s)	$\mu_k/\mu$
0-5	24.0	24.0	-	-
5-15	35.0	35.0	-	-
15-30	42.0	42.0	44.3	0.0
30-60	61.0	61.0	5.91	0.375
60-90	61.0	61.0	1.99	0.375
90-120	61.0	61.0	1.31	0.375
120-150	61.0	61.0	1.10	0.375
150- $\infty$	61.0	61.0	1.07	0.375

195 **Table 1.** Assumed and estimated material properties.  $\lambda$  and  $\mu$  are assumed known *a priori* and are based  
 196 on the values used for the coseismic model by Wei *et al.* [2011b]. The values for  $\eta_{\text{eff}}$  are estimated in Section  
 197 3.2, and  $\frac{\mu_k}{\mu}$  are the optimal shear moduli ratios found in Section 3.3 for a Zener rheology upper mantle.

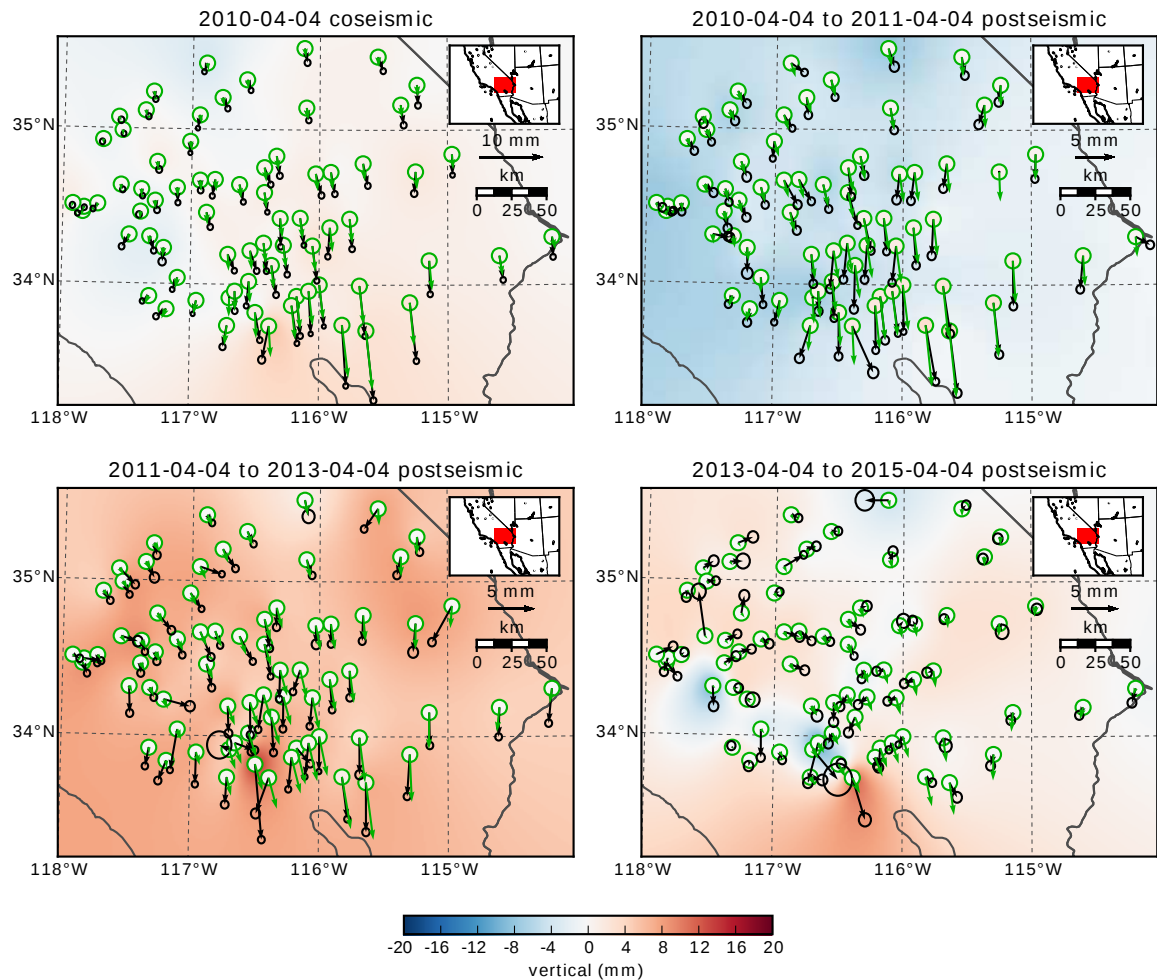


**Figure 5.** Same as Figure 4 but for far-field stations.

202 lastic rebound is unlikely to be a significant contributor to postseismic deformation following  
 203 the El Mayor-Cucapah earthquake. Furthermore, we consider stations which are sufficiently  
 204 far away from the main rupture that poroelastic rebound should be insignificant.

205 We estimate coseismic and time-dependent postseismic fault slip, both of which are as-  
 206 sumed to occur on a fault geometry modified from *Wei et al.* [2011b]. Field studies [*Fletcher*  
 207 *et al.*, 2014] and LIDAR observations [*Oskin et al.*, 2012] have revealed a significantly more  
 208 complicated fault geometry than what was inferred by *Wei et al.* [2011b], especially within the  
 209 Sierra Cucapah. However, we find that a relatively simple coseismic fault geometry based on  
 210 [*Wei et al.*, 2011b] is adequate because most of the stations used in this study are sufficiently  
 211 far from the El Mayor-Cucapah rupture zone that they are insensitive to the details in the fault  
 212 geometry found by *Fletcher et al.* [2014] and *Oskin et al.* [2012]. The fault geometry used in  
 213 this study (Figure 1) consists of the two main fault segments inferred by *Wei et al.* [2011b],  
 214 where the northern segment runs through the Sierra Cucapah up to the US-Mexico border and  
 215 the southern segment is the Indiviso fault which extends down to the Gulf of California. Both  
 216 segments extend from the surface to 15 km depth. We extend the northern segment by 40 km  
 217 to the north-west, motivated by the clustering of aftershocks on the northern tip of the coseis-  
 218 mic rupture zone [*Hauksson et al.*, 2011; *Kroll et al.*, 2013]. This extended fault segment was  
 219 also found to be necessary by *Rollins et al.* [2015] and *Pollitz et al.* [2012] in order to describe  
 220 the postseismic deformation.

### 221 3.1 Elastic Postseismic Inversion

We consider a variety of rheologic models for the lower crust and upper mantle. The simplest rheologic model is to consider them to be effectively elastic and isotropic. In such case, the rheologic parameters consist of the Lamé parameters,  $\lambda$  and  $\mu$ , which are reasonably well known and we use the same values used by *Wei et al.* [2011b] throughout this paper (Table 3). The only unknown is the distribution of fault slip, which can be easily estimated from postseismic deformation through linear least squares. Using a subset of the GPS stations considered in this study, *Rollins et al.* [2015] found that three years of postseismic deformation following the El Mayor-Cucapah earthquake can be explained with afterslip on the coseismic fault plane without requiring any viscoelastic relaxation. We also perform an elastic slip inversion, but we use GPS stations within a larger radius about the El Mayor-Cucapah epicenter (400 km instead of  $\sim$ 200 km). Our forward problem describing predicted postseismic deformation  $u_{\text{pred}}$  in terms of time dependent fault slip,  $s$ , is

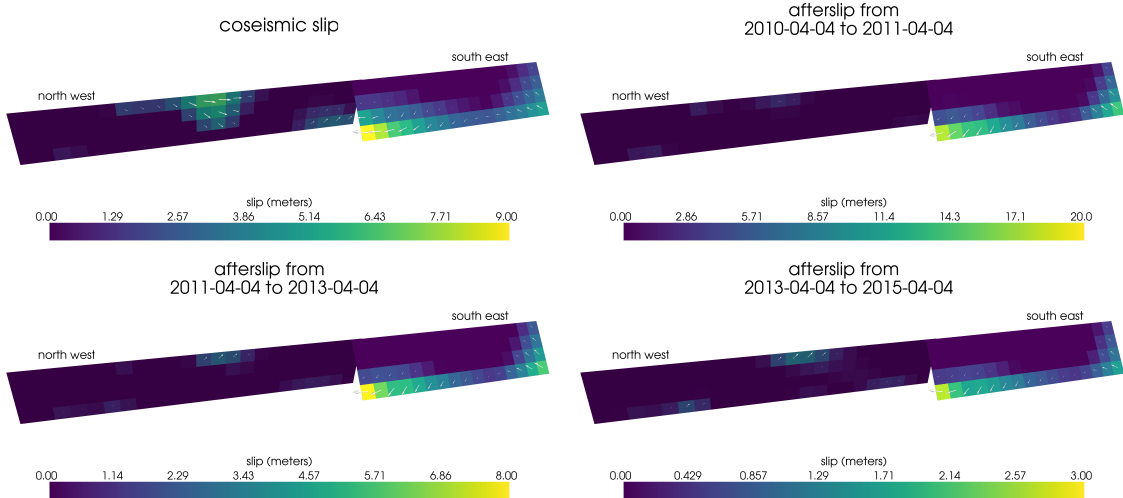
$$u_{\text{pred}}(x, t) = \int_F s(\xi, t) g(x, \xi) d\xi, \quad (9)$$

where  $F$  denotes the fault and  $g(x, \xi)$  is the elastic Green's function describing displacement at surface position  $x$  resulting from slip at  $\xi$  on the fault. We estimate coseismic slip and the rate of afterslip at the discrete time intervals, 0.0-0.125, 0.125-0.25, 0.5-1.0, 1.0-2.0, 2.0-3.0, 3.0-4.0, and 4.0-5.0 years after the earthquake. Each fault segment is discretized into roughly 4 km by 4 km patches and we estimate a strike-slip and thrust component of slip for each patch. We impose that the direction of slip and slip rate are within  $45^\circ$  of right-lateral. We also add zeroth-order Tikhonov regularization so that our solution for  $s$  satisfies

$$\min_s \left( \left\| \frac{u_{\text{pred}}(s) - u_{\text{post}}}{\sigma_{\text{post}}} \right\|_2^2 + \lambda_s \|s\|_2^2 \right), \quad (10)$$

222 where  $\sigma_{\text{post}}$  is the uncertainty on postseismic displacements and  $\lambda_s$  is a penalty parameter which  
 223 is chosen with a trade-off curve. We use Pylith [*Aagaard et al.*, 2013] to compute the Green's  
 224 functions for this inversion as well as for the remaining inversions in this paper.

225 Our coseismic slip and afterslip solutions are shown in Figure 6. As with *Rollins et al.*  
 226 [2015], we find that a large amount of afterslip on the southern fault segment is required to  
 227 explain the observations. The potency of our inferred coseismic slip is  $3.2 \times 10^9 \text{ m}^3$ , equiv-  
 228 alent to a Mw7.28 earthquake when assuming a shear modulus of 32 GPa. The potency of our



241 **Figure 6.** Coseismic slip and cumulative afterslip over the indicated intervals for the elastic model from  
242 Section 3.1. Color indicates the magnitude of slip while arrows indicate the motion of the hanging wall.

229 inferred cumulative five years of afterslip is  $6.1 \times 10^9 \text{ m}^3$ , equivalent to a Mw7.46 earthquake,  
230 which is unrealistically large if we consider afterslip to be driven by coseismically induced  
231 stresses. Figure 7 shows the time series for the observed and predicted postseismic displace-  
232 ments at stations along the El Mayor-Cucapah P axis. We show the radial component of dis-  
233 placements with respect to the El Mayor-Cucapah epicenter and we also rescale the displace-  
234 ments so that the difference between the minimum and maximum observed displacements are  
235 the same for each station. Our elastic slip model accurately describes near-field postseismic  
236 deformation and systematically underestimates postseismic deformation at epicentral distances  
237  $\gtrsim 150 \text{ km}$ . When the fault segments used in the inversion are extended down to 30 km depth,  
238 rather than 15 km, the systematic far-field residuals are smaller but remain apparent. Because  
239 an elastic model requires an unrealistic amount of afterslip and is unable to predict far-field  
240 deformation, we move on to consider viscoelastic models in the next section.

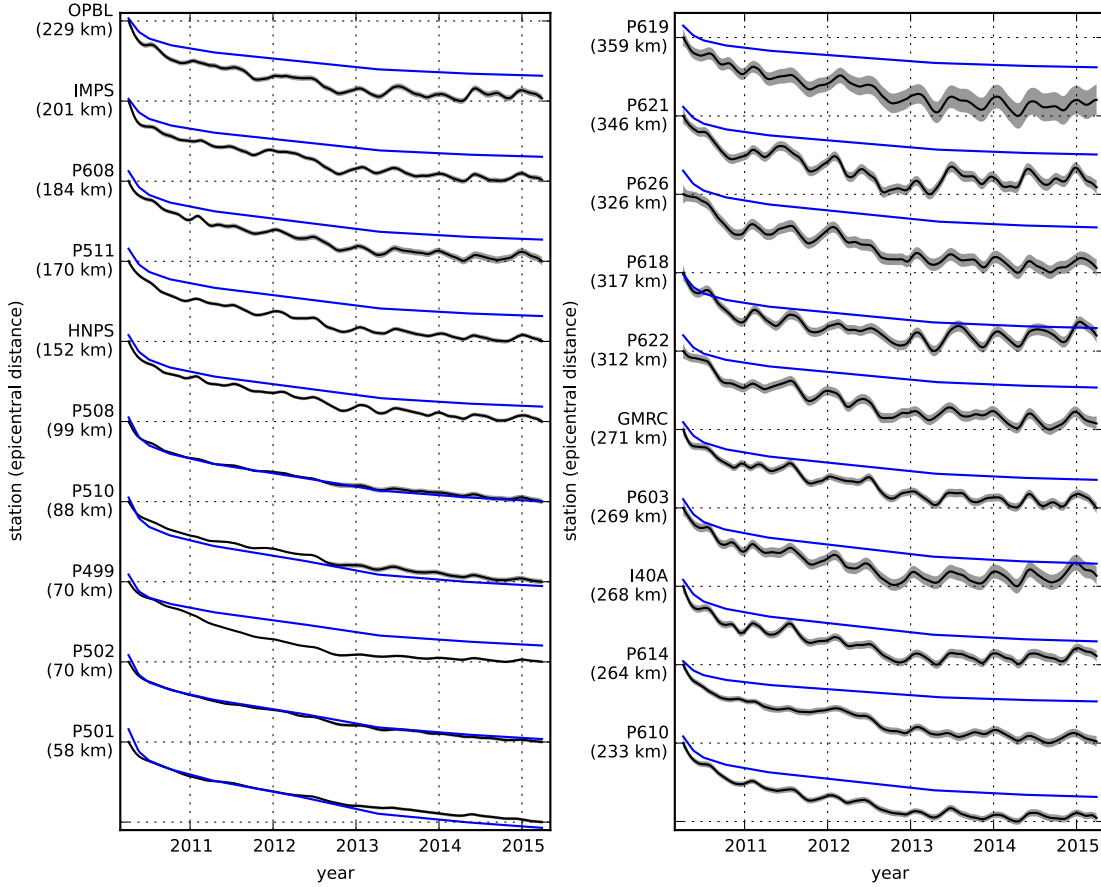
### 248 3.2 Early Postseismic Inversion

For any linear viscoelastic rheology of the crust and mantle, postseismic displacements  
resulting from time dependent fault slip can be described as

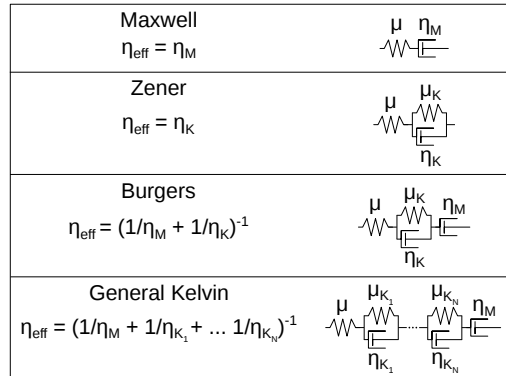
$$249 u_{\text{pred}}(x, t) = \int_F s(\xi, t) g(x, \xi) d\xi + \int_0^t \int_F s(\xi, \tau) f(t - \tau, x, \xi) d\xi d\tau, \quad (11)$$

250 where  $f(t, x, \xi)$  describes the time-dependent velocity at  $x$  resulting from viscoelastic relax-  
251 ation of stresses induced by slip at  $\xi$ .  $f$  is a function of  $\lambda$ ,  $\mu$ , and any additional rheologic pa-  
252 rameters controlling the viscoelastic response, which are generally not well known. Schematic  
253 representations of the viscoelastic rheologic models considered in this study are shown in Figure 8. We discuss these rheologic models and their use in geophysical studies in Section 4.

In order to greatly simplify the inverse problem, we use the method described in *Hines and Hetland* [2016] to constrain an initial effective viscosity structure from the early postseis-  
mic deformation. Our method utilizes the fact that coseismic stresses throughout the crust and  
upper mantle depend on the instantaneous elastic parameters and are independent of the vis-  
coelastic parameters which we wish to estimate. Immediately following an earthquake, each  
parcel will have a strain rate that is proportional to the coseismic stress and inversely propor-  
tional to the parcel's effective viscosity,  $\eta_{\text{eff}}$ . Using one-dimensional viscoelastic models, we



243 **Figure 7.** Scaled radial component of observed postseismic displacements  $u_{\text{obs}}$  (black) and displacements  
 244 predicted by the best fitting elastic model  $u_{\text{pred}}$  (blue). Downward motion indicates that the station is moving  
 245 toward the El Mayor-Cucapah epicenter. Displacement time series are scaled so that the minimum and maximum  
 246 observed values lie on the grid lines. The 68% confidence interval for the observed displacements are  
 247 shown in gray.



254 **Figure 8.** Schematic illustration of the rheologic models considered in this paper as well as their effective  
 255 viscosities.

define the effective viscosity as

$$\eta_{\text{eff}} = \frac{\sigma}{\dot{\varepsilon}} \Big|_{t=0}, \quad (12)$$

where  $\sigma$  is an applied stress at  $t = 0$  and  $\dot{\varepsilon}$  is the resulting strain rate. Figure 8 shows how  $\eta_{\text{eff}}$  relates to the parameters for various linear viscoelastic rheologies. We can deduce that the initial rate of surface deformation resulting from viscoelastic relaxation is a summation of the surface deformation resulting from relaxation in each parcel, scaled by the reciprocal of the parcel's effective viscosity. That is to say

$$f(0, x, \xi) = \int_L \frac{h(x, \xi, \zeta)}{\eta_{\text{eff}}(\zeta)} d\zeta, \quad (13)$$

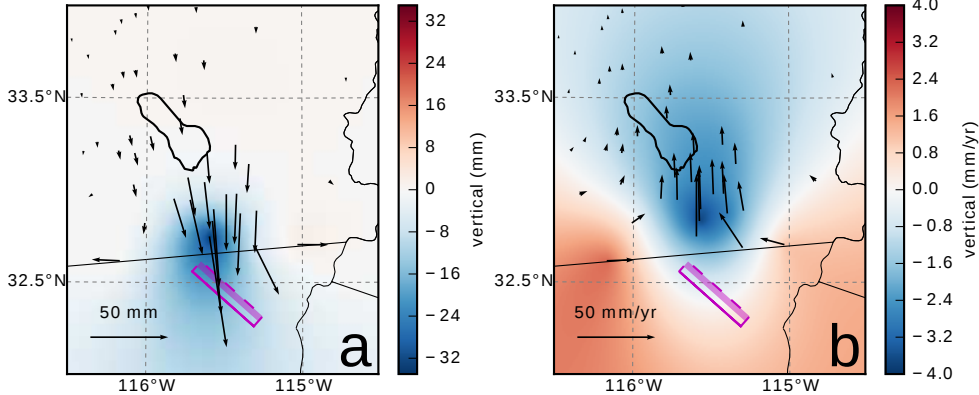
where  $L$  denotes the crust and mantle and  $h(x, \xi, \zeta)$  describes the initial rate of deformation resulting from viscoelastic relaxation at  $\zeta$  induced by slip at  $\xi$ . We can combine eq. (13) with eq. (11) to get a first order approximation for early postseismic deformation,

$$u_{\text{pred}}(x, t) \approx \int_F s(\xi, t) g(x, \xi) d\xi + \int_0^t \int_F \int_L \frac{s(\tau, \xi)}{\eta_{\text{eff}}(\zeta)} h(x, \xi, \zeta) d\zeta d\xi d\tau, \quad (14)$$

which is valid for as long as the rate of deformation resulting from viscoelastic relaxation is approximately constant. Although eq. (14) may only be valid for a short portion of the post-seismic period, its utility becomes apparent when noting that  $g$  and  $h$  are only functions of the fault geometry and instantaneous elastic properties,  $\lambda$  and  $\mu$ , and thus  $g$  and  $h$  can be computed numerically as a preprocessing step. The forward problem in eq. (14) can then be rapidly evaluated for any realization of  $s$  and  $\eta_{\text{eff}}$ . This is in contrast to evaluating the full forward problem, eq. (11), numerically for each realization of  $s$  and the unknown rheologic properties.

Details on how eq. (14) is used to estimate  $s$  and  $\eta_{\text{eff}}$  from postseismic deformation can be found in *Hines and Hetland* [2016]. A non-linear Kalman filter based inverse method can also be used to estimate  $s$  and  $\eta_{\text{eff}}$  in a manner akin to *Segall and Mathews* [1997] or *McGuire and Segall* [2003], in which we would not have to explicitly impose a time dependent parametrization of  $s$ . We have thoroughly explored Kalman filter based approaches, but we ultimately prefer the method described in *Hines and Hetland* [2016] because of its relative simplicity. Moreover, we believe the piecewise continuous representation of slip with respect to time to be sufficiently general for the resolving power of these GPS data.

We estimate coseismic slip and afterslip with the same spatial and temporal discretization as in Section 3.1. Simultaneously, we estimate  $\eta_{\text{eff}}$  within six vertically stratified layers which have depths ranging from 15-30 km, 30-60 km, 60-90 km, 90-120 km, 120-150 km, as well as from 150 km to the bottom of our numerical model domain at 800 km. We again restrict fault slip to occur between 0 and 15 km depth, which is done in order to help eliminate inevitable non-uniqueness in the inversion. It has long been recognized that fault slip at sufficiently great depths can produce surface deformation that is indistinguishable from viscoelastic relaxation, at least in two-dimensional earthquake models [Savage, 1990]. Additionally, we note that when simultaneously estimating both afterslip and viscosity in the lower crust, the inverse problem becomes particularly ill-posed. This ill-posedness is illustrated in Figure 9, which shows the displacements resulting from a meter of slip on a fault extending from 15 to 30 km depth and the initial velocity resulting from subsequent viscoelastic relaxation in the lower crust, which is given a viscosity of  $10^{18}$  Pa s. In this demonstration, the viscoelastic relaxation is entirely driven by the fault slip in the lower crust. The horizontal displacements from fault slip are in the opposite direction as the displacements resulting from viscoelastic relaxation. This means that surface displacements resulting from afterslip at lower crustal depths can be cancelled out, at least partially, by a low viscosity lower crust. We eliminate this null space by allowing only one mechanism in the lower crust, which we choose to be viscoelastic relaxation. This is not to say that we do not believe deep afterslip to be a possibility; rather, we restrict slip to seismogenic depths as a modeling necessity. Although, it has been noted that the pattern of vertical postseismic deformation following the El Mayor-Cucphuong earthquake indicates that a significant amount of afterslip must be shallow [Rollins *et al.*, 2015].



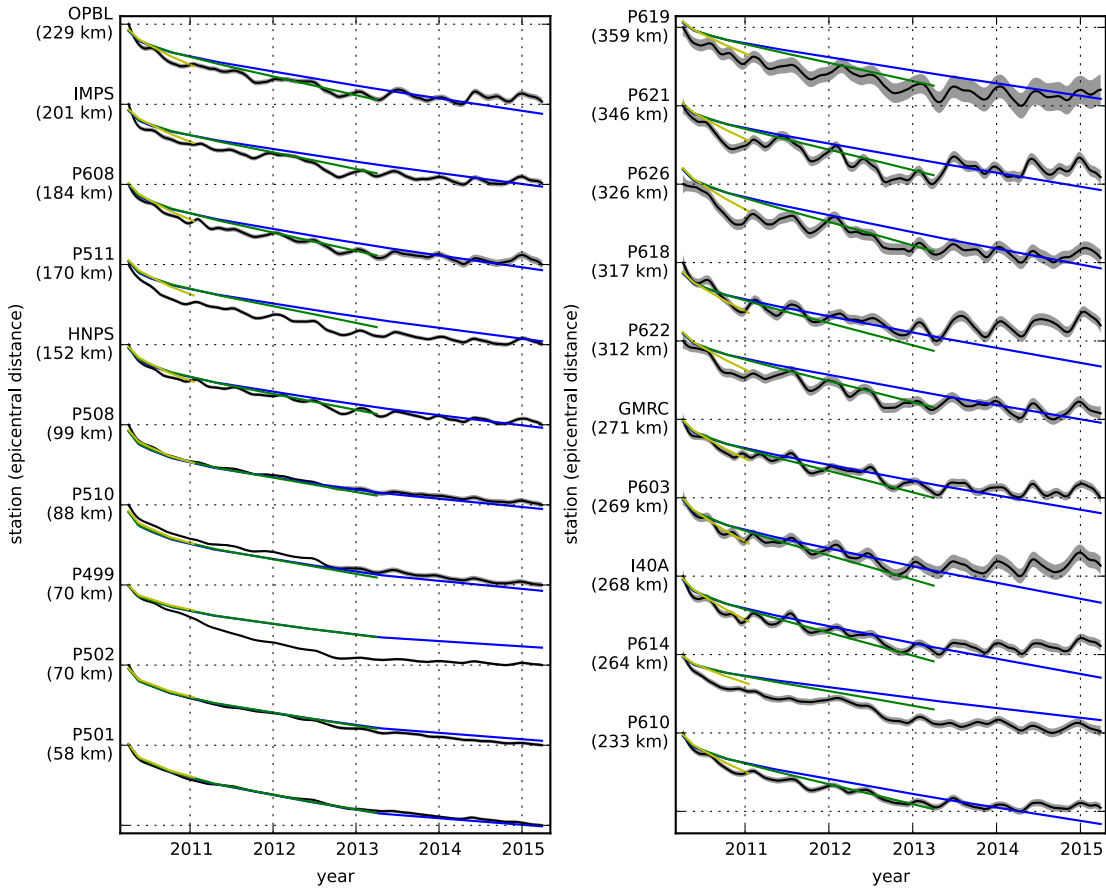
294 **Figure 9.** Displacements resulting from fault slip at lower crustal depths (a), and initial velocities resulting  
 295 from subsequent relaxation of a viscoelastic lower crust (b). The fault segment dips  $75^\circ$  to the north-east and  
 296 its surface projection is outlined in magenta. The highlighted area on the fault extends from 15 to 30 km depth  
 297 and indicates where 1 meter of right-lateral slip was imposed. The elastic properties of the crust and mantle  
 298 are the same as in Table 3, and  $\eta_{\text{eff}}$  is  $10^{18}$  Pa s in the lower crust. Vertical displacements are interpolated  
 299 between station locations.

300 We must determine at which point the early postseismic approximation breaks down, which  
 301 we will denote as  $t_{\text{bd}}$ . As noted, eq. (14) is valid for approximately as long as the rate of de-  
 302 formation resulting from viscoelastic relaxation is approximately constant. We can almost cer-  
 303 tainly assume that deformation at the most far-field stations, which are  $\sim 400$  km away from  
 304 the El Mayor-Cucapah epicenter, is the result of viscoelastic relaxation. The approxima-  
 305 tion should then be valid for as long as a linear trend adequately approximates the far-field de-  
 306 formation. Using this logic, it would appear that  $t_{\text{bd}}$  is about one year after the El Mayor-Cucapah  
 307 earthquake. Another way to determine  $t_{\text{bd}}$  is to find the best fitting prediction of eq. (14) to  
 308 observed deformation using increasing durations of the postseismic time series.  $t_{\text{bd}}$  should be  
 309 the point when eq. (14) is no longer capable of describing the observed deformation without  
 310 incurring systematic misfits. When using eq. (14) to fit the entire five years of postseismic dis-  
 311 placements, we see that the near-field displacements (e.g., station P501) are accurately pre-  
 312 dicted. When looking at displacements in the far-field (e.g., station P621), we see that eq. (14)  
 313 overestimates the rate of deformation in the later postseismic period and underestimates the  
 314 rate of deformation in the early period (Figure 10). Due to the low signal-to-noise ratios for  
 315 far-field stations, it is difficult to determine at what point eq. (14) is no longer able to predict  
 316 the observed displacements; however, we settle on  $t_{\text{bd}} = 0.8$  years after the earthquake, while  
 317 acknowledging that the choice is subjective. As noted in Hines and Hetland [2016], overes-  
 318 timating  $t_{\text{bd}}$  will result in a bias towards overestimating  $\eta_{\text{eff}}$ , while picking a  $t_{\text{bd}}$  which is too  
 319 low will not necessarily result in a biased estimate of  $\eta_{\text{eff}}$ , although the uncertainties would  
 320 be larger. We can then consider inferences of  $\eta_{\text{eff}}$  to be an upper bound on the viscosity needed  
 321 to describe the far-field rate of deformation during the first 0.8 years of postseismic deforma-  
 322 tion.

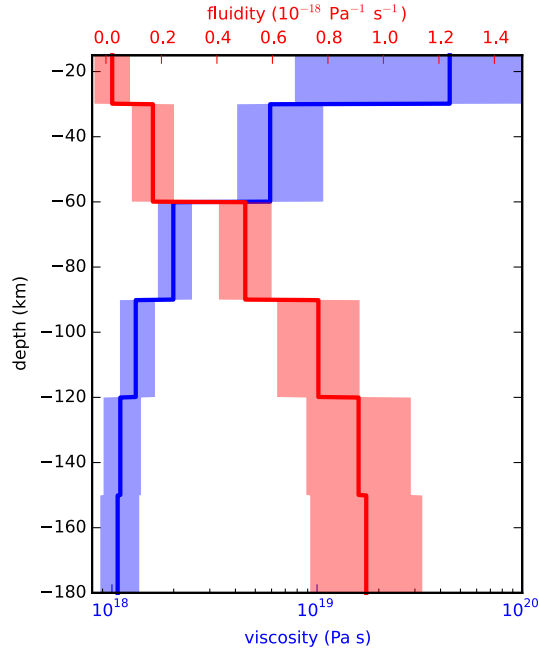
We estimate coseismic slip, afterslip, and effective viscosities by solving

$$\min_{s, \eta_{\text{eff}}} \left( \left\| \frac{u_{\text{pred}}(s, \eta_{\text{eff}}) - u_{\text{post}}}{\sigma_{\text{post}}} \right\|_2^2 + \lambda_s \|s\|_2^2 + \lambda_\eta \|\nabla \eta_{\text{eff}}^{-1}\|_2^2 \right), \quad (15)$$

325 where  $u_{\text{post}}$  consists of the first 0.8 years of postseismic deformation and  $u_{\text{pred}}$  are the pre-  
 326 dicted displacements from eq. (14). Due to inherent non-uniqueness, we have added zeroth-  
 327 order Tikhonov regularization to estimates of  $s$  and second-order Tikhonov regularization to  
 328 estimates of effective fluidity  $\eta_{\text{eff}}^{-1}$ . The degree to which we impose the regularization on slip



323 **Figure 10.** Observed postseismic displacements (black) and best fitting predictions of eq. (14) to 5.0 (blue),  
 324 3.0 (green), and 0.8 (yellow) years of the postseismic data.

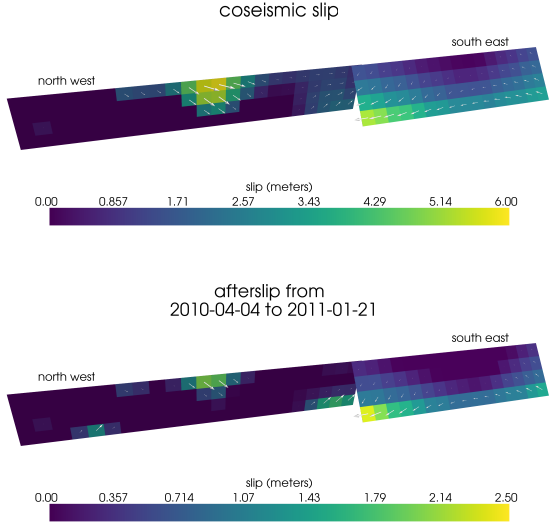


349 **Figure 11.** Effective viscosities and associated fluidities inferred by fitting eq. (14) to the first 0.8 years of  
 350 postseismic displacements. 95% confidence intervals, estimated from bootstrapping, are indicated by color  
 351 fields.

329 and fluidity is controlled by the penalty parameters  $\lambda_s$  and  $\lambda_\eta$ , which are chosen with trade-  
 330 off curves. Our goal here is to get a prior constraint on  $\eta_{\text{eff}}$  to minimize the amount of search-  
 331 ing we have to do when describing the postseismic deformation over the full five years, which  
 332 we do in Section 3.3. Estimates of  $s$  made here will not be used in Section 3.3, and so the  
 333 motivation behind adding regularization to  $s$  is to ensure that the slip driving viscoelastic re-  
 334 laxation in eq. (14) is sensible.

335 Our estimated effective viscosities, and corresponding fluidities, are shown in Figure 11.  
 336 Although fluidity is rarely used in geophysical literature, eq. (13) is linear with respect to flu-  
 337 idity and so the fluidity indicates the amplitude of the viscoelastic signal coming from each  
 338 layer. We also show the 95% confidence intervals for estimated viscosities and fluidities but  
 339 we note that the uncertainties tend to be underestimated due to the added regularization [Aster  
 340 *et al.*, 2011]. A robust feature that we see is that the largest jump in fluidity is at 60 km depth,  
 341 which is consistent with the range of lithosphere-asthenosphere boundary depths inferred by  
 342 Lekic *et al.* [2011]. This transitional depth is also consistent with the the viscosity structure  
 343 required to explain far-field postseismic deformation following the Hector Mine earthquake  
 344 [Freed *et al.*, 2007]. We find that the viscosity below 60 km depth needs to be  $\sim 10^{18}$  Pa s to  
 345 describe the early rate of postseismic deformation at far-field stations while the lower crust  
 346 and uppermost mantle need to be relatively stronger. The viscosity of the lower crust is the  
 347 least well constrained as there is no evidence of relaxation in that layer, meaning that it is ef-  
 348 fectively elastic over the first 0.8 years after the earthquake.

352 Our initial estimate for coseismic slip and cumulative afterslip over the first 0.8 years  
 353 after the El Mayor-Cucapah earthquake are shown in Figure 12. Similar to our elastic slip model  
 354 from Section 3.1, a significant amount of right-lateral and normal coseismic slip is inferred  
 355 to be on the Sierra Cucapah fault segment. Our coseismic slip solution is consistent with field  
 356 studies [Fletcher *et al.*, 2014] and the model from Wei *et al.* [2011b]. The potency of inferred  
 357 coseismic slip is  $3.3 \times 10^9$  m<sup>3</sup>, which is also about the same as that inferred from Section  
 358 3.1. The present inference of afterslip on the Indiviso fault is significantly less than what was



367 **Figure 12.** Coseismic slip and afterslip inferred by fitting eq. (14) to the first 0.8 years of postseismic  
368 displacements.

359 found in the Section 3.1 where we did not account for viscoelasticity. When fault slip is si-  
360 multaneously estimated with viscosity, the potency of inferred afterslip over the first 0.8 years  
361 after the earthquake is  $0.85 \times 10^9 \text{ m}^3$ , compared to  $3.5 \times 10^9 \text{ m}^3$  when we assume the crust  
362 and upper mantle are elastic. The significant amount of afterslip inferred on the Indiviso fault  
363 seems to be compensating for unmodeled viscoelastic relaxation at depths greater than 60 km.  
364 The fact that there is still an appreciable amount of afterslip inferred on the Indiviso fault raises  
365 the question of whether it is compensating for viscoelastic relaxation that is more localized  
366 than what we allow for since we only estimate depth dependent variations in viscosity.

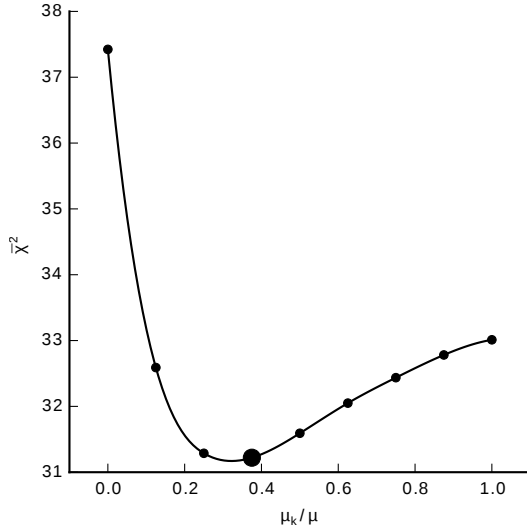
### 369 3.3 Full Postseismic Inversion

In the previous section, we used the inverse method from *Hines and Hetland* [2016] to constrain the effective viscosity structure required to explain the first 0.8 years of postseismic deformation. In this section, we use these effective viscosities as a prior constraint when searching for models which are capable of describing the available five years of postseismic data, where our forward problem is now eq. (11) rather than the approximation given by eq. (14). We perform a series of fault slip inversions assuming a variety of rheologies for the lower crust and upper mantle which are consistent with our findings from Section 3.2. We appraise each model using the mean chi-squared value,

$$370 \bar{\chi}^2 = \frac{1}{N} \left\| \frac{u_{\text{pred}} - u_{\text{obs}}}{\sigma_{\text{obs}}} \right\|_2^2, \quad (16)$$

where  $N$  is the number of observations.

We first assume that the crust and mantle can be described with a Maxwell rheology, and we set the steady-state viscosity  $\eta_M$  equal to our inference of  $\eta_{\text{eff}}$ . We compute  $f$  and  $g$  from eq. (11) using Pylith, and we use the same spatial and temporal discretization of  $s$  as in Sections 3.1 and 3.2. We estimate  $s$  using linear least squares and find a misfit of  $\bar{\chi}^2 = 37.4$ . For comparison,  $\bar{\chi}^2 = 35.3$  for the elastic model from Section 3.1. The Maxwell viscoelastic model has a larger misfit because it tends to overestimate the rate of deformation after about three years (Figure 14). Since our initial estimates of  $\eta_{\text{eff}}$  may be biased towards overestimating viscosities, we have also performed the slip inversion where we use uniformly lower



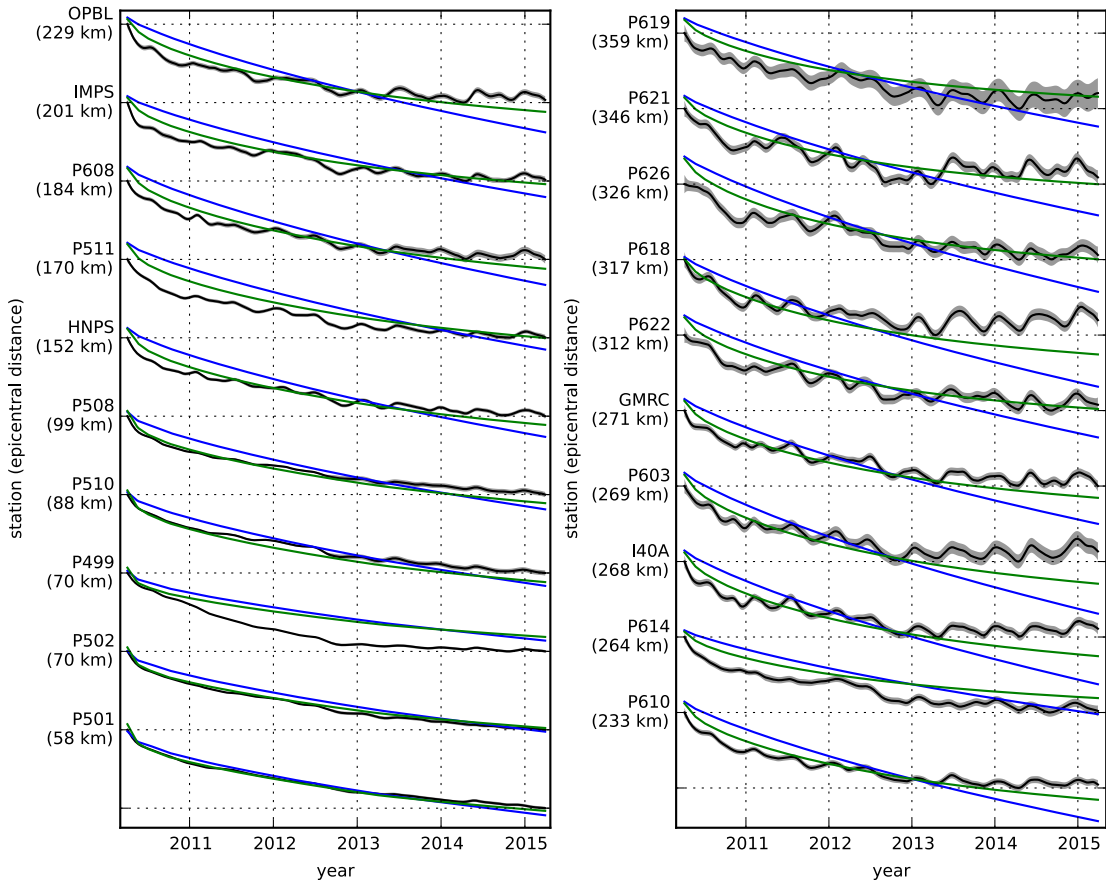
400      **Figure 13.** Mean chi-squared value for the best fitting slip model as a function of the transient shear modu-  
401      lus relative to the elastic shear modulus in a Zener upper mantle. Large dot indicates our preferred ratio.

379      viscosities in the crust and mantle. However, decreasing the viscosity only increases the mis-  
380      fit. Although, the viscosities used here are consistent with the successful Maxwell viscoelas-  
381      tic models found by *Rollins et al.* [2015] and *Spinler et al.* [2015], which had mantle viscosities  
382      on the order of  $10^{18}$  Pa s and relatively higher lower crustal viscosities, we find that such  
383      a model is incapable of describing the entire postseismic time series. *Pollitz et al.* [2001] simi-  
384      larly recognized this deficiency in a Maxwell rheology, which then motivated their exploration  
385      of a Burgers rheology upper mantle [*Pollitz*, 2003].

386      Instead of exploring a Burgers rheology mantle, which introduces two new parameters  
387      that need to be estimated, the transient viscosity  $\eta_K$  and transient shear modulus  $\mu_K$ , we first  
388      consider a Zener rheology for the mantle, which only introduces one additional unknown pa-  
389      rameter,  $\mu_K$ . We assume that the lower crust still has a Maxwell rheology. The steady-state  
390      viscosity in the crust and the transient viscosity in the mantle are set equal to the inferred ef-  
391      fective viscosities. We then estimate the ratio of shear moduli  $\frac{\mu_K}{\mu}$ . We compute nine differ-  
392      ent sets of Green's functions,  $f$  and  $g$ , where we assume values of  $\frac{\mu_K}{\mu}$  ranging from 0 to 1.  
393      The former being a degenerate case where the Zener model reduces to the above Maxwell model.  
394      We estimate coseismic slip and afterslip for each realization of  $\frac{\mu_K}{\mu}$ . The shear moduli ratio  
395      that yields the best prediction to the observed postseismic displacements is found to be 0.375  
396      which produces a misfit of  $\bar{\chi}^2 = 31.2$  (Figure 13). The improvement in the Zener model over  
397      the Maxwell model can be clearly seen in the fit to the far-field data (Figure 14). The Zener  
398      model does a significantly better job at explaining the transient rate of far-field deformation  
399      throughout the five years.

407      Because we are able to adequately describe the available five years of postseismic de-  
408      formation with a Zener model, we do not find it necessary to explore the parameter space for  
409      a more complicated Burgers rheology. However, since the Zener model is a Burgers model with  
410      an infinite steady-state viscosity, we can conclude that any Burgers rheology that has a trans-  
411      ient viscosity consistent with that found in Section 3.2 and a steady-state viscosity  $\gtrsim 10^{20}$   
412      Pa s, which is effectively infinite on the time scale of five years, would also be able to sat-  
413      isfactorily describe the observable postseismic deformation.

414      The regularized inference of coseismic slip and afterslip for our preferred Zener model  
415      is shown in Figure 15. The inferred coseismic potency is  $3.0 \times 10^9$  m<sup>3</sup>, equivalent to a Mw7.26  
416      earthquake, and most of the slip is shallow and on the Sierra Cucapah fault segment. The po-



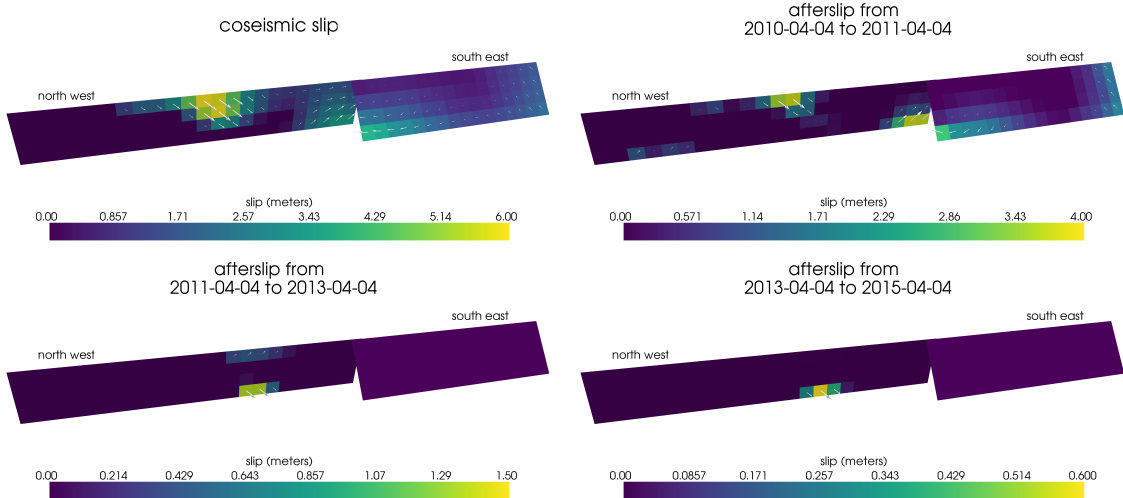
402 **Figure 14.** Observed postseismic displacements (black). Predicted postseismic displacements for the best  
 403 fitting slip model when assuming a Maxwell viscoelastic lower crust and upper mantle (blue). Predicted post-  
 404 seismic displacements for the best fitting slip model when assuming a Maxwell viscoelastic lower crust and a  
 405 Zener viscoelastic upper mantle (green). The effective viscosities are the same for both models and are shown  
 406 in Figure 11.

tency of five years of afterslip is  $1.1 \times 10^9$  m<sup>3</sup>. Most of the afterslip in our preferred model occurs within the first year after the earthquake and coincides with the location of our inferred coseismic slip. Inferred afterslip within the first year is accounting for the most rapid near-field transient deformation. After one year, afterslip is inferred to be deeper down on the Sierra Cucapah segment, which is describing much of the sustained near-field postseismic deformation. We emphasize, that the GPS station closest to where we infer afterslip, P496, is still about 30 km away, which is too far for us to conclusively argue for sustained localized deformation rather than shallow distributed deformation. The deep afterslip inferred after one year could potentially be describing deformation resulting from lower crustal flow. To test this, we have modified our preferred model by decreasing the lower crustal viscosity from  $5.91 \times 10^{19}$  Pa s to  $1 \times 10^{19}$  Pa s, which is still consistent with our viscosity inference from Section 3.2, and inverted for fault slip. We find that a model with a weaker lower crust adequately describes the postseismic displacements without any afterslip after one year, while still requiring about the same amount of afterslip over the first year. We do believe that the early shallow afterslip on the Sierra Cucapah segment is a robust feature in our preferred model, while we are not confident in our inference of later deep afterslip.

the postseismic displacements predicted by our preferred model are shown in Figures 4, 5 and 14. Overall, the trends in the near-field and far-field transient deformation are accurately described. In particular, the trends in far-field deformation are much better described by our preferred Zener model than either an elastic model or a model with a Maxwell viscoelastic mantle (Figure 14). There are a few areas where we have notable misfit. Most of our misfit is for the near-field stations in the Imperial Valley, and we attribute this misfit to our relatively simple fault geometry, which does not account for potential fault slip in the Imperial Valley triggered by the El Mayor-Cucapah earthquake [Wei *et al.*, 2011a, 2015]. In particular, we are unable to model the sustained, rapid rate of deformation at station P496, which suggests that this station could be influenced by a more localized deformation mechanism than is considered in this study. Additionally, we see systematic misfit in the later postseismic period west of the Landers and Hector Mine earthquakes, which may be the result of unmodeled postseismic deformation resulting from those earthquakes. Lastly, there are clear discrepancies between the observed and predicted vertical deformation following the first year after the El Mayor Cucapah earthquake. We observe a broad uplift throughout Southern California, which is inconsistent with any postseismic model.

## 4 Discussion

It has long been recognized that deep afterslip and viscoelastic relaxation following an upper crustal earthquake can result in similar horizontal ground deformation at the surface [e.g. Savage, 1990; Pollitz *et al.*, 2001; Hearn, 2003; Feigl and Thatcher, 2006]. The similarity of the horizontal postseismic deformation results in a non-uniqueness in inferences of afterslip or viscoelastic relaxation. In contrast, the spatial pattern of vertical postseismic deformation has been proposed to be a discriminant between deep afterslip and viscoelastic relaxation [e.g. Pollitz *et al.*, 2001; Hearn, 2003]. It is, however, important to note that patterns of vertical deformation are very sensitive to the depth-dependence of viscosity below the upper crust [Yang and Toksöz, 1981; Hetland and Zhang, 2014]. The similarity between deformation resulting from deep afterslip and viscoelastic relaxation of coseismic stresses is different from the ill-posedness described in Section 3.2. In our method, any inferred afterslip will also mechanically drive additional viscoelastic relaxation. The horizontal deformation resulting from deep afterslip will generally be in the opposite direction as horizontal deformation resulting from viscoelastic relaxation of subsequent stresses in the lower crust (Figure 9). As a result, there is a trade-off between inferences of deep afterslip and lower crustal viscosity. In our synthetic tests in Hines and Hetland [2016], we have found that inverting surface deformation for afterslip and viscosity within the same depth interval tends to result in overestimated afterslip and an underestimated viscosity.



449 **Figure 15.** Inferred coseismic slip and afterslip when assuming a Maxwell rheology in the lower crust and  
 450 a Zener rheology in the upper mantle. The transient viscosity  $\eta_K$  in the mantle and steady-state viscosity  $\eta_M$   
 451 in the crust are set equal to the effective viscosities from Figure 11. We set  $\frac{\mu_K}{\mu} = 0.375$  in the upper mantle.

471 Most postseismic studies assume Maxwell viscoelasticity in the lower crust and upper  
 472 mantle [e.g. *Nur and Mavko*, 1974; *Pollitz et al.*, 2000; *Hetland*, 2003; *Freed et al.*, 2006; *Johnson et al.*, 2009; *Hearn et al.*, 2009], which is the simplest viscoelastic rheologic model. In South-  
 473 ern California, postseismic studies following the Landers [*Pollitz et al.*, 2000], Hector Mine  
 474 [*Pollitz et al.*, 2001], and El Mayor-Cucapah earthquake [*Spinler et al.*, 2015; *Rollins et al.*, 2015],  
 475 have assumed Maxwell viscoelasticity in the lower crust and upper mantle and have inferred  
 476 upper mantle viscosities on the order of  $10^{17}$  to  $10^{18}$  Pa s and lower crust viscosities  $\gtrsim 10^{19}$   
 477 Pa s. These postseismic studies are consistent with *Kaufmann and Amelung* [2000] and *Cava-  
 478 lié et al.* [2007], who found that an upper mantle viscosity of  $10^{18}$  Pa s and a crustal viscosity  
 479  $\gtrsim 10^{20}$  Pa s are necessary to describe subsidence resulting from changes in loading from  
 480 Lake Mead. This isostatic adjustment is a process with similar spatial and temporal scales as  
 481 postseismic deformation, and thus the inferred viscosities of these two types of studies would  
 482 likely agree. While these studies found viscosities that are consistent with our effective vis-  
 483 cosities from Section 3.2, they are inconsistent with viscosity estimates made from geophys-  
 484 ical processes that occur over longer time scales. For example, *Lundgren et al.* [2009] found  
 485 that lower crust and upper mantle viscosities on the order of  $10^{21}$  and  $10^{19}$  Pa s, respectively,  
 486 are needed to describe interseismic deformation along the Southern San Andreas fault zone  
 487 in the Salton Sea region. An even higher mantle viscosity, on the order of  $10^{20}$  Pa s, is re-  
 488 quired to describe isostatic adjustment resulting from the draining of Lake Bonneville, which  
 489 occurs on the time scales of  $10^4$  years [*Crittenden*, 1967; *Bills and May*, 1987].

490 An additional deficiency with the Maxwell rheology is that it predicts a steady decay  
 491 in the rate of postseismic deformation over time, which fails to describe the commonly ob-  
 492 served rapid, early transience followed by a relatively steady rate of postseismic deformation.  
 493 One could explain the early transient postseismic deformation with fault creep and the later  
 494 phase with relaxation in a Maxwell viscoelastic lower crust and upper mantle [e.g. *Hearn et al.*,  
 495 2009; *Johnson et al.*, 2009]. However, postseismic deformation at distances greater than  $\sim 200$   
 496 km from the El Mayor-Cucapah epicenter can only be attributed to viscoelastic relaxation [*Freed  
 497 et al.*, 2007] and we have demonstrated that the far-field deformation cannot be explained with  
 498 a Maxwell rheology (Figure 14).

We found that a Zener rheology in the upper mantle with a transient viscosity of  $\sim 10^{18}$  Pa s does a noticeably better job at predicting far-field postseismic deformation. A generalization of the Zener viscoelastic model, schematically represented as several Kelvin elements connected in series, is commonly used to describe seismic attenuation [Liu *et al.*, 1976]. The highest viscosity needed to describe seismic attenuation is on the order of  $10^{16}$  Pa s [Yuen and Peltier, 1982] which has a characteristic relaxation time on the order of days. Even though our inferred transient viscosity is orders of magnitude larger than that required for seismic attenuation models, the two models are not incompatible. Rather, the delayed elasticity in seismic attenuation models occurs on such short time scales that it can be considered part of the instantaneous elastic phase of deformation associated with the preferred Zener model in this study.

Of course, it has long been recognized that a Zener rheology provides an incomplete descriptions of the asthenosphere, as it does not have the fluid-like behavior required to explain isostatic rebound or convection in the mantle [O'Connell, 1971]. Yuen and Peltier [1982] proposed a Burgers rheology with a low transient viscosity ( $\eta_K \approx 10^{16}$  Pa s) and high steady-state viscosity ( $\eta_M \approx 10^{21}$  Pa s) to describe both seismic attenuation and long term geologic processes. The justification of a Burger's rheology mantle is further supported by laboratory experiments on olivine [Chopra, 1997]. Pollitz [2003] sought to describe postseismic deformation following Hector Mine with a Burgers rheology mantle and they found a best fitting transient viscosity of  $1.6 \times 10^{17}$  Pa s and steady-state viscosity of  $4.6 \times 10^{18}$  Pa s. While the Burgers rheology was introduced as a means of bridging the gap between relaxation observed in long and short term geophysical processes, the inferred steady state viscosity from Pollitz [2003] is still inconsistent with the Maxwell viscosities inferred from studies on the earthquake cycle and Lake Bonneville. The transient viscosity inferred by Pollitz [2003] is constrained by the earliest phase of postseismic deformation following the Hector Mine earthquake. While Pollitz [2003] ruled out deep afterslip as an alternative mechanism based on inconsistent vertical deformation, it is still possible to successfully describe all components of early postseismic deformation following the Hector Mine earthquake with afterslip at seismogenic depths [Jacobs *et al.*, 2002]. It is then possible that the preferred rheologic model from Pollitz [2003] was biased towards inferring a particularly low transient viscosity by neglecting to account for afterslip. This is in contrast to the present study, where we have inferred a viscosity structure simultaneously with afterslip. We also argue that a transient rheology is necessary to explain postseismic deformation; however, our preferred transient viscosity of  $\sim 10^{18}$  Pa s in the upper mantle is an order of magnitude larger than the transient viscosity found by Pollitz [2003]. Since a Zener model is able to describe the available postseismic deformation following the El Mayor-Cucapah earthquake, any Burgers rheology with a steady-state viscosity that is  $\gtrsim 10^{20}$  Pa s, effectively infinite over five years, would also be able to describe the postseismic deformation. Such a Burgers model might then be consistent with the steady-state viscosities necessary for lake loading, interseismic deformation, and mantle dynamics.

## 5 Conclusion

We have extracted a filtered and smoothed estimate of postseismic deformation following the El Mayor-Cucapah earthquake from GPS displacement time series. We treated postseismic deformation as a stochastic process where we did not presume any characteristic shape of the postseismic time series. Our estimated postseismic deformation reveals far-field (epicentral distances beyond  $\sim 200$  km) transient deformation which is largely undetectable after about three years. Near-field deformation exhibits transience that decays to a sustained, elevated rate after about one or two years. We found that near-field transient deformation can be explained with shallow afterslip, and the sustained rate of near-field deformation can either be explained with continued afterslip or relaxation in a lower crustal with a viscosity of  $\sim 10^{19}$  Pa s. Far-field transient deformation can be more definitively ascribed to viscoelastic relaxation at depths greater than  $\sim 60$  km. Beneath that depth, a transient viscosity of  $\sim 10^{18}$  Pa s is required to describe the rate of far-field deformation throughout the five years considered

552 in this study. By describing the available postseismic deformation with a transient rheology  
 553 in the mantle, our preferred model does not conflict with the generally higher steady-state vis-  
 554 cosities inferred from geophysical processes occurring over longer time scales.

555 **Acknowledgements**

556 We thank Andy Freed for an illuminating discussion on the data used in this study. This  
 557 material is based on EarthScope Plate Boundary Observatory data services provided by UN-  
 558 AVCO through the GAGE Facility with support from the National Science Foundation (NSF)  
 559 and National Aeronautics and Space Administration (NASA) under NSF Cooperative Agree-  
 560 ment No. EAR-1261833. This material is based upon work supported by the National Science  
 561 Foundation under Grant Numbers EAR 1045372 and EAR 1245263.

562 **References**

- 563 Aagaard, B. T., M. G. Knepley, and C. A. Williams (2013). A domain decomposition  
 564 approach to implementing fault slip in finite-element models of quasi-static and dy-  
 565 namic crustal deformation, *Journal of Geophysical Research: Solid Earth*, 118, doi:  
 566 10.1002/jgrb.50217.
- 567 Argus, D. F., M. B. Heflin, G. Peltzer, F. Crampé, and F. H. Webb (2005), Interseismic  
 568 strain accumulation and anthropogenic motion in metropolitan Los Angeles, *Journal of*  
 569 *Geophysical Research: Solid Earth*, 110(4), 1–26, doi:10.1029/2003JB002934.
- 570 Aster, R. C., B. Borchers, and C. H. Thurber (2011), Parameter Estimation and Inverse  
 571 Problems, vol. 90, Academic Press.
- 572 Bawden, G. W., W. Thatcher, R. S. Stein, K. W. Hudnut, and G. Peltzer (2001), Tectonic  
 573 contraction across Los Angeles after removal of groundwater pumping effects., *Nature*,  
 574 412(August), 812–815, doi:10.1038/35090558.
- 575 Bills, B. G., and G. M. May (1987), Lake Bonneville: Constraints on Lithospheric Thick-  
 576 ness and Upper Mantle Viscosity From Isostatic Warping of Bonneville, Provo, and  
 577 Gilbert Stage Shorelines, *Journal of Geophysical Research-Solid Earth and Planets*,  
 578 92(B11), 11,493–11,508, doi:10.1029/JB092iB11p11493.
- 579 Çakir, Z., S. Ergintav, H. Özener, U. Dogan, A. M. Akoglu, M. Meghraoui, and  
 580 R. Reilinger (2012), Onset of aseismic creep on major strike-slip faults, *Geology*,  
 581 40(12), 1115–1118, doi:10.1130/G33522.1.
- 582 Cavalié, O., M. P. Doin, C. Lasserre, and P. Briole (2007), Ground motion measurement in  
 583 the Lake Mead area, Nevada, by differential synthetic aperture radar interferometry time  
 584 series analysis: Probing the lithosphere rheological structure, *Journal of Geophysical*  
 585 *Research: Solid Earth*, 112(3), 1–18, doi:10.1029/2006JB004344.
- 586 Cetin, E., Z. Cakir, M. Meghraoui, S. Ergintav, and A. M. Akoglu (2014), Extent and  
 587 distribution of aseismic slip on the Işmetpasa segment of the North Anatolian Fault  
 588 (Turkey) from Persistent Scatterer InSAR, *Geochemistry, Geophysics, Geosystems*, 15,  
 589 doi:10.1002/2014GC005307.Received.
- 590 Chopra, P. N. (1997), High-temperature transient creep in olivine rocks, *Tectonophysics*,  
 591 279, 93–111, doi:10.1016/S0040-1951(97)00134-0.
- 592 Crittenden, M. (1967), Viscosity and Finite Strength of the Mantle as Determined from  
 593 Water and Ice Loads\*, *Geophysical Journal of the Royal Astronomical ...*, pp. 261–279,  
 594 doi:10.1111/j.1365-246X.1967.tb06243.x.
- 595 Davis, J. L., B. P. Wernicke, and M. E. Tamisiea (2012), On seasonal signals in geode-  
 596 tic time series, *Journal of Geophysical Research: Solid Earth*, 117(1), 1–10, doi:  
 597 10.1029/2011JB008690.
- 598 Feigl, K. L., and W. Thatcher (2006), Geodetic observations of post-seismic transients in  
 599 the context of the earthquake deformation cycle, *Comptes Rendus - Geoscience*, 338,  
 600 1012–1028, doi:10.1016/j.crte.2006.06.006.

- 601 Fletcher, J. M., O. J. Teran, T. K. Rockwell, M. E. Oskin, K. W. Hudnut, K. J. Mueller,  
 602 R. M. Spelz, S. O. Akciz, E. Masana, G. Faneros, E. J. Fielding, S. Leprince, A. E.  
 603 Morelan, J. Stock, D. K. Lynch, A. J. Elliott, P. Gold, J. Liu-Zeng, A. González-  
 604 Ortega, A. Hinojosa-Corona, and J. González-García (2014), Assembly of a large  
 605 earthquake from a complex fault system: Surface rupture kinematics of the 4 April  
 606 2010 El Mayor-Cucapah (Mexico) Mw 7.2 earthquake, *Geosphere*, *10*(4), 797–827,  
 607 doi:10.1130/GES00933.1.
- 608 Freed, A. M., R. Bürgmann, E. Calais, J. Freymueller, and S. Hreinsdóttir (2006), Impli-  
 609 cations of deformation following the 2002 Denali, Alaska, earthquake for postseismic  
 610 relaxation processes and lithospheric rheology, *Journal of Geophysical Research: Solid*  
 611 *Earth*, *111*, 1–23, doi:10.1029/2005JB003894.
- 612 Freed, A. M., R. Bürgmann, and T. Herring (2007), Far-reaching transient motions after  
 613 Mojave earthquakes require broad mantle flow beneath a strong crust, *Geophysical*  
 614 *Research Letters*, *34*, 1–5, doi:10.1029/2007GL030959.
- 615 Gonzalez-Ortega, A., Y. Fialko, D. Sandwell, F. A. Nava-pichardo, J. Fletcher,  
 616 J. Gonzalez-garcia, B. Lipovsky, M. Floyd, and G. Funning (2014), El Mayor-  
 617 Cucapah (Mw7.2) earthquake: early near-field postseismic deformation from In-  
 618 Sar and GPS observations, *Journal of Geophysical Research*, *119*, 1482–1497, doi:  
 619 10.1002/2013JB010193.Received.
- 620 Hauksson, E., J. Stock, K. Hutton, W. Yang, J. A. Vidal-Villegas, and H. Kanamori  
 621 (2011), The 2010 Mw 7.2 El mayor-cucapah earthquake sequence, Baja Califor-  
 622 nia, Mexico and Southernmost California, USA: Active seismotectonics along the  
 623 Mexican pacific margin, *Pure and Applied Geophysics*, *168*(3918), 1255–1277, doi:  
 624 10.1007/s00024-010-0209-7.
- 625 Hearn, E. H. (2003), What can GPS data tell us about the dynamics of post-seismic defor-  
 626 mation ?, (2003), 753–777.
- 627 Hearn, E. H., S. McClusky, S. Ergintav, and R. E. Reilinger (2009), Izmit earthquake post-  
 628 seismic deformation and dynamics of the North Anatolian Fault Zone, *Journal of Geo-*  
 629 *physical Research: Solid Earth*, *114*(August 2008), 1–21, doi:10.1029/2008JB006026.
- 630 Hetland, E. A. (2003), Postseismic relaxation across the Central Nevada Seismic Belt,  
 631 *Journal of Geophysical Research*, *108*(Figure 2), 1–13, doi:10.1029/2002JB002257.
- 632 Hetland, E. A., and G. Zhang (2014), Effect of shear zones on post-seismic deformation  
 633 with application to the 1997 Mw 7.6 manyi earthquake, *Geophysical Journal Interna-*  
 634 *tional*, *198*, 259–269, doi:10.1093/gji/ggu127.
- 635 Hines, T. T., and E. A. Hetland (2013), Bias in estimates of lithosphere viscosity from  
 636 interseismic deformation, *Geophysical Research Letters*, *40*(16), 4260–4265, doi:  
 637 10.1002/grl.50839.
- 638 Hines, T. T., and E. A. Hetland (2016), Rapid and simultaneous estimation of fault slip  
 639 and heterogeneous lithospheric viscosity from post-seismic deformation, *Geophysical*  
 640 *Journal International*, *204*(1), 569–582, doi:10.1093/gji/ggv477.
- 641 Jacobs, A., D. Sandwell, Y. Fialko, and L. Sichoix (2002), The 1999 (Mw7.1) Hector  
 642 Mine, California, Earthquake: Near-Field Postseismic Deformation from ERS Interfer-  
 643 ometry, *Bulletin of the Seismological Society of America*, *92*(May), 1433–1442.
- 644 Johnson, K. M., and P. Segall (2004), Viscoelastic earthquake cycle models with deep  
 645 stress-driven creep along the San Andreas fault system, *Journal of Geophysical Research*  
 646 *B: Solid Earth*, *109*, 1–19, doi:10.1029/2004JB003096.
- 647 Johnson, K. M., R. Bürgmann, and J. T. Freymueller (2009), Coupled afterslip and vis-  
 648 coelastic flow following the 2002 Denali Fault, Alaska earthquake, *Geophysical Journal*  
 649 *International*, *176*(3), 670–682, doi:10.1111/j.1365-246X.2008.04029.x.
- 650 Jónsson, S., P. Segall, R. Pedersen, and G. Bjornsson (2003), Post-earthquake ground  
 651 movements correlated to pore-pressure transients, *Nature*, *424*(July), 179–183, doi:  
 652 10.1038/nature01758.1.
- 653 Kaufmann, G., and F. Amelung (2000), Reservoir-induced deformation and continental  
 654 rheology in vicinity of Lake Mead, Nevada, *Journal of Geophysical Research*, *105*(B7),

- 655            16,341, doi:10.1029/2000JB900079.
- 656       Kroll, K. A., E. S. Cochran, K. B. Richards-Dinger, and D. F. Sumy (2013), Aftershocks  
 657       of the 2010 Mw 7.2 El Mayor-Cucapah earthquake reveal complex faulting in the Yuha  
 658       Desert, California, *Journal of Geophysical Research: Solid Earth*, 118(October), 6146–  
 659       6164, doi:10.1002/2013JB010529.
- 660       Lekic, V., S. W. French, and K. M. Fischer (2011), Lithospheric Thinning Beneath Rifted  
 661       Regions of Southern California, *Science*, 334(November), 783–787.
- 662       Liu, H.-P., D. L. Anderson, and H. Kanamori (1976), Velocity dispersion due to anelasticity;  
 663       implications for seismology and mantle composition, *Geophysical Journal International*,  
 664       47(1), 41–58, doi:10.1111/j.1365-246X.1976.tb01261.x.
- 665       Lundgren, P., E. A. Hetland, Z. Liu, and E. J. Fielding (2009), Southern San Andreas-San  
 666       Jacinto fault system slip rates estimated from earthquake cycle models constrained by  
 667       GPS and interferometric synthetic aperture radar observations, *Journal of Geophysical  
 668       Research: Solid Earth*, 114(2), 1–18, doi:10.1029/2008JB005996.
- 669       McGuire, J. J., and P. Segall (2003), Imaging of aseismic fault slip transients recorded  
 670       by dense geodetic networks, *Geophysical Journal International*, 155(3), 778–788, doi:  
 671       10.1111/j.1365-246X.2003.02022.x.
- 672       Meade, B. J., and B. H. Hager (2005), Block models of crustal motion in southern Cali-  
 673       fornia constrained by GPS measurements, *Journal of Geophysical Research B: Solid  
 674       Earth*, 110, 1–19, doi:10.1029/2004JB003209.
- 675       Murray, J. R., and P. Segall (2005), Spatiotemporal evolution of a transient slip event on  
 676       the San Andreas fault near Parkfield, California, *Journal of Geophysical Research : Solid  
 677       Earth*, 110(9), 1–12, doi:10.1029/2005JB003651.
- 678       Nur, A., and G. Mavko (1974), Postseismic viscoelastic rebound, *Science*, 183(4121),  
 679       204–206, doi:10.1038/098448b0.
- 680       O'Connell, R. J. (1971), Rheology of the Mantle, *EOS, Transactions, American Geophysi-  
 681       cal Union*, 52, 140–142.
- 682       Oskin, M. E., J. R. Arrowsmith, A. Hinojosa Corona, A. J. Elliott, J. M. Fletcher, E. J.  
 683       Fielding, P. O. Gold, J. J. Gonzalez Garcia, K. W. Hudnut, J. Liu-Zeng, and O. J. Teran  
 684       (2012), Near-field deformation from the El Mayor-Cucapah earthquake revealed by  
 685       differential LIDAR, *Science*, 335(6069), 702–705, doi:10.1126/science.1213778.
- 686       Pollitz, F., C. Wicks, and W. Thatcher (2001), Mantle Flow Beneath a Continental Strike-  
 687       Slip Fault : Postseismic Deformation After the 1999 Hector Mine Earthquake, *Science*,  
 688       1814(2001), 1814–1818, doi:10.1126/science.1061361.
- 689       Pollitz, F. F. (2003), Transient rheology of the uppermost mantle beneath the Mo-  
 690       jave Desert, California, *Earth and Planetary Science Letters*, 215, 89–104, doi:  
 691       10.1016/S0012-821X(03)00432-1.
- 692       Pollitz, F. F., G. Peltzer, and R. Bürgmann (2000), Mobility of continental mantle: Evi-  
 693       dence from postseismic geodetic observations following the 1992 Landers earthquake,  
 694       *Journal of Geophysical Research*, 105(1999), 8035, doi:10.1029/1999JB900380.
- 695       Pollitz, F. F., R. Bürgmann, and W. Thatcher (2012), Illumination of rheological mantle  
 696       heterogeneity by the M7.2 2010 El Mayor-Cucapah earthquake, *Geochemistry, Geo-  
 697       physics, Geosystems*, 13(6), 1–17, doi:10.1029/2012GC004139.
- 698       Rauch, H. E., F. Tung, and C. T. Striebel (1965), Maximum likelihood estimates of linear  
 699       dynamic systems, *AIAA Journal*, 3(8), 1445–1450.
- 700       Riva, R. E. M., and R. Govers (2009), Relating viscosities from postseismic relaxation to  
 701       a realistic viscosity structure for the lithosphere, *Geophysical Journal International*, 176,  
 702       614–624, doi:10.1111/j.1365-246X.2008.04004.x.
- 703       Rollins, C., S. Barbot, and J.-P. Avouac (2015), Postseismic Deformation Following the  
 704       2010 M7.2 El Mayor-Cucapah Earthquake : Observations , Kinematic Inversions , and  
 705       Dynamic Models, *Pure and Applied Geophysics*, doi:10.1007/s00024-014-1005-6.
- 706       Savage, J. C. (1990), Equivalent strike-slip earthquake cycles in half-space and  
 707       lithosphere-asthenosphere earth models, *Journal of Geophysical Research*, 95, 4873,  
 708       doi:10.1029/JB095iB04p04873.

- 709 Savage, J. C., and J. L. Svarc (2009), Postseismic relaxation following the 1992 M 7.3  
710 Landers and 1999 M 7.1 Hector Mine earthquakes , southern California, *Journal of*  
711 *Geophysical Research*, 114(B01401), doi:10.1029/2008JB005938.
- 712 Savage, J. C., J. L. Svarc, and S. B. Yu (2005), Postseismic relaxation and transient creep,  
713 *Journal of Geophysical Research: Solid Earth*, 110, 1–14, doi:10.1029/2005JB003687.
- 714 Segall, P., and M. Mathews (1997), Time dependent inversion of geodetic data, *Journal of*  
715 *Geophysical Research*, 102.
- 716 Spinler, J. C., R. A. Bennett, C. Walls, L. Shawn, and J. J. G. Garcia (2015), As-  
717 sessing long-term postseismic deformation following the M7.2 4 April 2010, El  
718 Mayor-Cucapah earthquake with implications for lithospheric rheology in the  
719 Salton Trough, *Journal of Geophysical Research: Solid Earth*, 120, 3664–3679, doi:  
720 10.1002/2014JB011613.Received.
- 721 Wei, M., D. Sandwell, Y. Fialko, and R. Bilham (2011a), Slip on faults in the Imperial  
722 Valley triggered by the 4 April 2010 Mw 7.2 El Mayor-Cucapah earthquake revealed by  
723 InSAR, *Geophysical Research Letters*, 38(January), 1–6, doi:10.1029/2010GL045235.
- 724 Wei, M., Y. Liu, Y. Kaneko, J. J. McGuire, and R. Bilham (2015), Dynamic triggering of  
725 creep events in the Salton Trough, Southern California by regional M5.4 earthquakes  
726 constrained by geodetic observations and numerical simulations, *Earth and Planetary  
727 Science Letters*, 427, 1–10, doi:10.1016/j.epsl.2015.06.044.
- 728 Wei, S., E. Fielding, S. Leprince, A. Sladen, J.-P. Avouac, D. Helmberger, E. Hauksson,  
729 R. Chu, M. Simons, K. Hudnut, T. Herring, and R. Briggs (2011b), Superficial sim-  
730 plicity of the 2010 El MayorCucapah earthquake of Baja California in Mexico, *Nature  
731 Geoscience*, 4(9), 615–618, doi:10.1038/ngeo1213.
- 732 Yang M., and M. N. Toksöz (1981), Time-dependent deformation and stress relaxation  
733 after strike-slip earthquakes, *Journal of Geophysical Research*, 86, 2889–2901.
- 734 Yuen, D. A., and W. R. Peltier (1982), Normal modes of the viscoelastic earth, *Geo-  
735 physical Journal of the Royal Astronomical Society*, 69, 495–526, doi:10.1111/j.1365-  
736 246X.1982.tb04962.x.